Biophysical Journal
Article

Biophysical Society

Measurement of Mesoscale Conformational Dynamics of Freely Diffusing Molecules with Tracking FCS

Charles Limouse,[1] Jason C. Bell,[2] Colin J. Fuller,[2] Aaron F. Straight,[2,*] and Hideo Mabuchi[1,*]
[1]Department of Applied Physics and [2]Department of Biochemistry, Stanford University, Stanford, California

ABSTRACT Few techniques are suited to probe the structure and dynamics of molecular complexes at the mesoscale level (~100–1000 nm). We have developed a single-molecule technique that uses tracking fluorescence correlation spectroscopy (tFCS) to probe the conformation and dynamics of mesoscale molecular assemblies. tFCS measures the distance fluctuations between two fluorescently labeled sites within an untethered, freely diffusing biomolecule. To achieve subdiffraction spatial resolution, we developed a feedback scheme that allows us to maintain the molecule at an optimal position within the laser intensity gradient for fluorescence correlation spectroscopy. We characterized tFCS spatial sensitivity by measuring the Brownian end-to-end dynamics of DNA molecules as short as 1000 bp. We demonstrate that tFCS detects changes in the compaction of reconstituted nucleosome arrays and can assay transient protein-mediated interactions between distant sites in an individual DNA molecule. Our measurements highlight the applicability of tFCS to a wide variety of biochemical processes involving mesoscale conformational dynamics.

INTRODUCTION

The regulation of gene expression, intracellular transport, replication, and many intracellular processes is mediated by the dynamics of molecular systems occurring at the mesoscale level (~100–1000 nm). Yet, methods for probing dynamics of mesoscale molecules are sparse. Super-resolution microscopy techniques (1) and biochemical methods to identify proximal interactions in vivo such as Hi-C (2,3), proximity-dependent biotin identification (4), or spatially restricted enzymatic tagging (5) are powerful tools that can provide a static view of mesoscale organization inside the cell. However, it would be highly valuable to complement these methods with approaches that can 1) report on dynamic changes in the conformation of mesoscale systems and 2) be applied to reconstituted systems, in which the dynamics of individual molecules can be measured in isolation or with selected partners and biochemical and biophysical models can be directly tested. Single-molecule methods that have been used to study mesoscale systems include tethered particle motion (6,7) and force spectroscopy (8,9). To our knowledge, we have developed a new approach that enables the measurement of conformational fluctuations in mesoscale biological molecules in tether-free and force-free conditions.

Tracking fluorescence correlation spectroscopy (tFCS) is a method that combines confocal microscopy, feedback-based single-molecule tracking, and fluorescence correlation spectroscopy (FCS) to measure the conformational dynamics of individual molecules without the need for mechanical tethering (10–14). The key element in tFCS is the use of active feedback to compensate for center of mass diffusion by repositioning the microscope stage in real time so that the fluorescence from an individual molecule can be monitored over a long period. However, tFCS has previously been restricted to very large molecules such as λ-phage DNA (15) (radius of gyration ~1 μm) because of spatial resolution limitations. Other active tracking methods (16–18) have been developed to measure hydrodynamic mobilities (19,20), stoichiometry of molecular complexes (21), or nanoscale conformational dynamics (22,23), but none has permitted mesoscale intramolecular dynamics measurements.

Here, we developed a dual-color tFCS method that specifically assays the distance fluctuations between two discrete sites within a single macromolecule with ~100–150 nm spatial resolution and sub-millisecond

---

Submitted July 12, 2017, and accepted for publication January 2, 2018.

*Correspondence: astraigh@stanford.edu or hmabuchi@stanford.edu

Editor: Anatoly Kolomeisky.
https://doi.org/10.1016/j.bpj.2018.01.044

temporal resolution. By optimizing the focal position of the lasers used for tracking and for intramolecular dynamics detection, we showed that tFCS has sufficient spatial and temporal resolution to probe the relative motion between two sites in freely diffusing DNA molecules separated by as little as 1000 bp. Additionally, we showed that tFCS can detect conformational transitions in diffusing chromatin fibers and DNA-looping processes induced by lac repressor. These measurements provide, to our knowledge, the first demonstration that tFCS can measure dynamic biophysical processes occurring on a subdiffraction scale, which has important implications for many molecular systems, particularly the dynamics of nucleoprotein systems.

MATERIALS AND METHODS

Single-molecule tracking microscope

To track individual molecules, we used a custom-built confocal microscope augmented with a feedback loop as well as beam-steering capabilities that enabled high-bandwidth electronic control of the position of the focus of each laser beam in the sample (details in Supporting Materials and Methods). Briefly, to achieve all-optical sensing of the three-dimensional (3D) position of the diffusing particle and real-time tracking, we set up the tracking laser according to the optical and feedback scheme previously described (13). To increase the tracking bandwidth of the instrument, we used two pairs of acousto-optic deflectors (AODs) placed in the path of the tracking and probe beams (Fig. 1 *A*) to serve as fast actuators, with microsecond-scale response time. This strategy allowed us to apply feedback faster than the mechanical resonance frequency of the piezo stage (∼100 Hz) and minimize the tracking localization error, which is key to resolving intramolecular dynamics at the subdiffraction limit scale.

Measurements conditions

All tFCS measurements were taken with molecules at ∼ 1 pM concentration so that one individual molecule drifted in the microscope confocal volume every ∼15–30 s, making it unlikely that two molecules were tracked at once. All of the DNA and LacI experiments were done in 10 mM Tris (pH 7.4), 50 mM KCl. The arrays data were taken in 10 mM Tris (pH 7.4), 25 mM NaCl, and either 2 mM MgCl (+ $MgCl_2$ conditions) or 0.5 mM EDTA (no $MgCl_2$ conditions). All buffers were complemented with an oxygen-scavenging system consisting of 0.01 units/mL of protocatechuate-dioxygenase, 2 mM of protocatechuic acid, and 1 mM of aged Trolox to serve as a reducing oxidizer system (24,25). For tFCS, 25 μL of sample was loaded into a microfluidic channel formed by two microscope cover slips (40 × 20 #1) separated by two overlaid layers of double-sided tape (3 M) positioned to create a narrow channel (∼3 × 20 × 0.3 mm, channel volume ∼15–20 μL). For the LacI and chromatin arrays experiments, the channels were passivated by incubation of a 1 mg mL^{-1} solution of casein for 5 min and rinsed with 100 μL of buffer before sample loading.

tFCS data recording and preprocessing

For each experiment, we collected data in continuous mode for 10–30 min, during which we recorded the fluorescence signal from the reference and probe dyes using the time-interval-analyzer board (GT653; GuideTech, Sunnyvale, CA) operating in time-tagged mode. The microscope stage trajectory and the tracking laser power were digitized at 1 kHz (National Instruments, Austin, TX). The reference-dye fluorescence was locked at $\sim 100\,\mathrm{kPhotons/s}$, and the red laser power was chosen to achieve a probe-dye fluorescence rate of $50-\ 100\,\mathrm{kPhotons/s}$. The raw signals were semiautomatically preprocessed offline to detect and classify

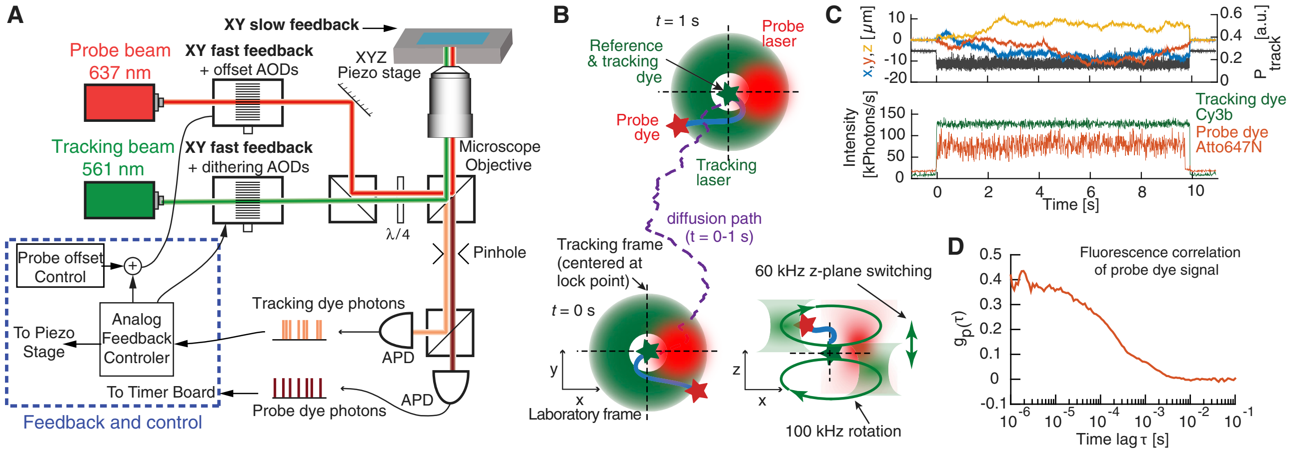

FIGURE 1 Instrumentation and concept of the tFCS assay. (*A*) Key optical and electronic elements of the tFCS microscope are shown. The feedback is applied by an analog controller (*blue box*), which drives the microscope piezo stage and the acousto-optic deflectors (AODs) controlling the position of the tracking and probe beams. The optical elements used to dither the tracking laser axially are omitted for simplification (Supporting Materials and Methods). (*B*) A schematic of the tracking and probe beam motions during tracking of a freely diffusing molecule is shown (*blue*). The trajectory (*purple line*) of the green-labeled site on the molecule (*green star*, reference dye) is followed by the tracking laser (*green beam*), whereas the probe laser (*red beam*) is maintained at a fixed position with respect to the tracking laser. The green ring indicates circular dithering of the tracking beam used to locate the molecule in XY (13). The focus of the rotating tracking laser is also axially dithered between two transverse planes to locate the molecule along the *z* axis (*bottom right*) (13). The green-labeled site is immobile with respect to the probe laser (at the tracking/reference lock point, *dashed crosshair*), whereas the red-labeled site (*red star*, probe dye) moves because of intramolecular dynamics. (*C*) Single-molecule signals recorded in tFCS are shown, including the probe fluorescence (*red*), the stage trajectory, and the tracking laser power (*black*), which is under feedback control to keep the tracking dye fluorescence at a fixed value (*green*). (*D*) A single-molecule fluorescence correlation function $g_p(\tau)$ from the probe signal in (*C*) is shown. To see this figure in color, go online.

individual molecules, compute the fluorescence correlation functions, and correct for background effects (Supporting Materials and Methods).

Compaction scores and clustering of conformational states

To compare molecular macrostates, tFCS data were quantified using a simple metric of molecular compaction. We defined the relative compaction between two molecules as the ratio of the inverse of the integral of the correlation function of the two molecules, computed over the interval of time lags from 5 ms to 5 μs. These bounds were chosen empirically to encompass the region of the correlation signal, which differs between the macrostates of interest, while avoiding introduction of noise from the shorter (<5 μs) and longer (>5 ms) timescales.

DNA constructs labeling and nucleosome arrays reconstitution

The DNA molecules used in all the experiments were fluorescently labeled with a single probe dye and a single reference dye by ligation or polymerase chain reaction. Nucleosome arrays were reconstituted using the salt dialysis method with purified H3/H4/H2A/H2B octamers, as previously described (26) (Supporting Materials and Methods).

RESULTS

Design of the tFCS assay to measure the intramolecular dynamics of freely diffusing single molecules

To measure the conformation of biological macromolecules in the absence of mechanical perturbation, we custom-designed a confocal microscope with a feedback system that compensates for the motion of individual molecules as they freely diffuse (13). The feedback system allows us to track single molecules for several seconds in 3D space while simultaneously observing their fluorescence emissions (Fig. 1 *A*). We tailored the system to specifically assay the distance and distance fluctuations between two parts of a single molecule or complex. To accomplish this, we used a green reference dye (Cy3b) as a reference point for tracking the movement of the molecule in three dimensions and a red probe dye (Atto647N) as a reporter of the intramolecular dynamics. We then controlled, via feedback, the position of two lasers in real time to simultaneously excite the reference tracking and probe dyes. To follow the diffusive path of the reference dye in the transverse plane (XY, perpendicular to the propagation axis), we dithered the tracking laser beam around a circular orbit at 100 kHz to generate a particle-position-dependent modulation of the dye fluorescence signal (Supporting Material; (11,27)). To track the displacement of the particle in the axial direction (Z), we dithered the axial focus of the rotating tracking laser at 65 kHz between two planes slightly above and below the focal plane of the probe laser (Supporting Material; (13)). Importantly, we coordinated the positions of the probe and tracking lasers in the XY plane (Fig. 1 *B*) to effectively maintain the probe laser focus at a fixed point relative to the reference site of the molecule. With this tFCS assay, which uses a dual-focus orbital tracking system and a two-fluorophore labeling scheme, we were able to collect ~1 million photons per molecule in both fluorescence channels (Fig. S1; Table S2).

Readout of the intramolecular dynamics

The schematic representation of a typical trajectory of the molecule and the focal positions of the lasers (Fig. 1 *B*) highlights how intramolecular dynamics results in a motion of the probe dye within the probe beam. Fluctuations of the probe fluorescence thus encode the 3D motion of the probe dye. Because the probe laser is spatially locked with respect to the reference dye, the tFCS measurement is only sensitive to the relative motion of the probe dye with respect to the reference dye, not to the overall center of mass diffusion nor to a static configuration in which the reference-to-probe dye vector is frozen (for example, if the molecule is immobilized).

However, because the molecule is free to tumble and rotate around the reference dye during tracking, the orientation of the reference-to-probe dye vector is never static in tFCS; therefore, even a rigid molecule with a fixed reference-to-probe dye distance exhibits fluorescence fluctuations that contain information about this distance (Fig. S2).

To quantify the reference-to-probe dye dynamics, we computed the autocorrelation of the probe dye fluorescence signal, as is standard in conventional FCS (Fig. 1, *C* and *D*). Given a model describing the motion of the probe dye and its blinking dynamics, it is theoretically possible to fit the tFCS signal and quantitatively estimate the model parameters, such as the amplitude and relaxation time of the intramolecular dynamics, but this approach is challenging (Discussion and Supporting Material Appendix). In this manuscript, we examined the amplitude of the tFCS signals of individual molecules as an uncalibrated readout of the amplitude of the reference-to-probe dye dynamics (Supporting Material Appendix; Fig. S6). Additionally, from the 3D movement of the molecule over time provided by the *X*, *Y*, and *Z* stage trajectory (Fig. 1 *C*), we obtained an independent and calibrated readout of the diffusion coefficient. Our approach is generalizable to any biological macromolecule that can be labeled with two different fluorophores. The labeling sites can be located on the same individual molecule or on two separate binding partners. Thus, by selecting the appropriate position of the reference and probe dyes, we can measure the dynamics between any pairs of sites within a macromolecular complex or even the distance between the sites of a rigid molecule by leveraging the rotational diffusion of the molecule.

Optimization of the spatial sensitivity of tFCS through optimization of the illumination geometry

A major challenge for mesoscale measurements is that the target resolution (~100 nm) is smaller than the size of the diffraction-limited probe beam. In prior implementations of tFCS, the intramolecular motion was larger than the beam dimensions, and the fluorescence fluctuations stemmed from large excursions of the probe dye in and out of the entire Gaussian beam profile (15). In this new tFCS assay, the trajectory of the probe dye samples only a small region of the illumination volume. To resolve intramolecular dynamics in the subdiffraction-limit regime, we increased the spatial sensitivity of the assay by configuring the feedback to maintain the molecule at the edge of the Gaussian profile of the probe laser, where the local intensity gradient is large (Fig. 2 *B*). If the reference and probe beams were co-linear (centered-illumination), the local intensity gradient seen by the probe fluorophore would be small, and intramolecular dynamics would give rise to small fluorescence fluctuations (Fig. 2 *A*). Therefore, we modified the microscope optical path so that the probe beam was laterally offset with respect to the tracking beam. We tuned the distance between the probe and tracking beam electronically using the AODs in the probe beam path (Fig. 1 *A*). With this "side-illumination" configuration, even small displacements of the probe dye result in large changes in the laser intensity seen by the probe dye, which provides a sensitive way to convert molecular motion into fluorescence fluctuations (Fig. S3).

Effect of tracking-localization error and experimental considerations for fast feedback

To obtain a high spatial resolution, it is essential that the microscope feedback loop tracks the displacement of the reference dye as accurately as possible. In practice, the actuator bandwidth and the finite dye brightness set limits on the feedback bandwidth and tracking accuracy (11). This leads to a residual motion of the probe dye in the probe beam, which impairs spatial sensitivity, as this is equivalent to random displacements of the probe beam away from its optimal position and reduces the local intensity gradient seen by the probe dye (Fig. 2 *C*).

To maximize tracking accuracy, we improved the feedback architecture so that we could track the molecule with a bandwidth larger than the resonance frequency of the piezo stage (~100 Hz). To do so, we implemented in the *XY* dimensions a feedback loop with two branches. We corrected for low-frequency components of the particle motion via feedback on the microscope piezo stage, whereas higher bandwidth components were canceled via feedback on the laser position, controlled with AODs. With this scheme, we were able to feedback at ~1 kHz bandwidth for *XY* tracking and maintain the reference dye within better than 100 nm of the desired lock point (root mean-square (RMS) error) for molecules diffusing up to 15 μm^2/s.

Numerical estimation of the spatial resolution of tFCS

To estimate the smallest distance fluctuations that can be resolved by tFCS and obtain a theoretical lower-bound on the tFCS resolution, we first conducted numerical simulations of the assay. We simulated tFCS signals for intramolecular dynamics, where the reference-to-probe dye distance fluctuates with a root mean-square distance (RMSD)

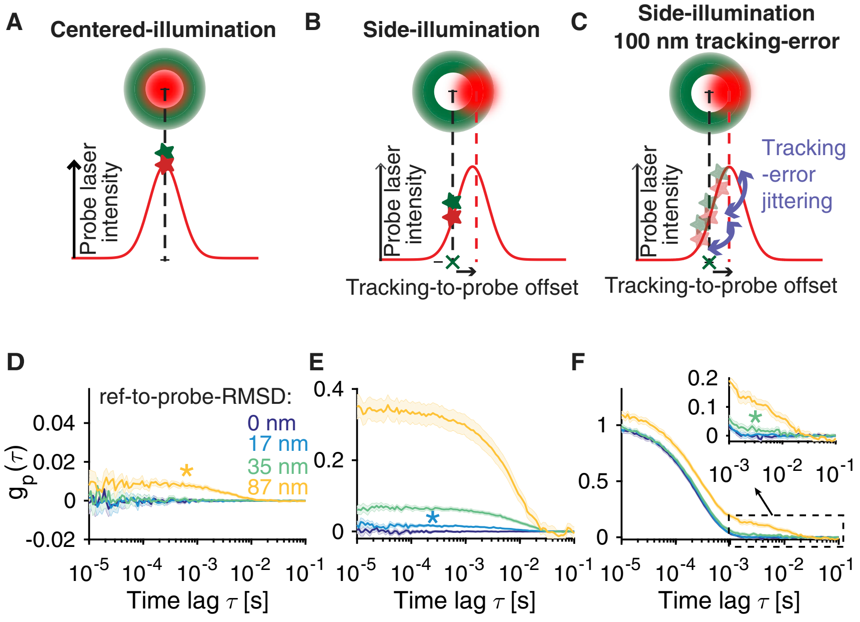

FIGURE 2 Optimization of tFCS spatial sensitivity with side-illumination, and expected resolution in presence of tracking localization error. (*A* and *B*) A schematic of the centered- (*A*) and side-illumination (*B*) configurations is shown. Top: the relative positions of the tracking (*green*) and probe (*red*) beams are shown. Bottom: the *X* axis cross-section of the probe laser intensity profile seen by the probe dye is shown. The green cross represents the lock point of the feedback (at the center of tracking laser circular orbit) with respect to which the reference dye is immobile. The green and red stars represent the average position of the reference and probe dyes in the beam, respectively. (*C*) The illustration shows the effect of finite-bandwidth tracking, in which the reference dye is imperfectly maintained at the lock point, which results in a residual jitter of the probe dye in the probe beam frame. (*D* and *E*) Simulated tFCS signals (mean ± 95% confidence interval) of molecules with a reference-to-probe dye root mean-square distance (RMSD) of 0, 17, 35, or 87 nm are shown, using either the centered- (*D*) or the side-illumination (*E*) configuration. In the side-illumination geometry, the reference-to-probe beam offset was set to 1.0 *w*, where *w* = 310 nm. Asterisk color indicates the shortest resolvable reference-to-probe RMSD. (*F*) The same simulation as that in (*E*) is shown, but this time taking into account imperfect feedback (100 nm RMS localization error). To see this figure in color, go online.

ranging from 17 to 87 nm (Fig. 2, *D–F*) and a characteristic timescale of 10 ms. The number of photons collected per molecule ($N = 500,000$), signal-to-noise ($s/n = 5$), and duration of tracking trace ($T = 5$ s) were chosen to represent typical experimental values (Fig. S1; Table S2). We then compared the tFCS signal obtained for each reference-to-probe RMSD with that of control molecules where the reference and probe sites were colocalized (i.e., reference-to-probe RMS distance equals 0). The simulated tFCS signals matched well with the theoretical prediction (Supporting Material Appendix Eq. 35) and allowed us to characterize the measurement noise and the resolution. In the ideal case of perfect tracking, the side-illumination configuration was able to resolve the intramolecular dynamics of all the molecules ranging from 17 nm and upward (Fig. 2 *E*), compared with the centered-illumination geometry, where only molecules with a reference-to-probe RMS distance of 87 nm were resolved (Fig. 2 *D*). When we accounted for a realistic tracking localization RMS error of 100 nm, the resolution was reduced to 35 nm with the side-illumination configuration (Fig. 2 *F*). Simulations with different intramolecular timescales of motion (1 and 10 ms) yielded similar results (Fig. S4), indicating that the resolution is not strongly dependent on the dynamics timescale.

To characterize the performance of tFCS in measuring the intramolecular dynamics of larger molecules, we next simulated signals from molecules with an RMSD ranging from 100 to 1000 nm. The time intervals in which the probe dye explores the focus of the probe beam become sparse, but the tFCS signal remains quantifiable (Fig. S5). Theoretical analysis of the tFCS amplitude indicates that as the end-to-end dynamics amplitude reaches the order of the beam dimension, the illumination geometry becomes irrelevant, and centered- and side-illumination geometry lead to similar correlation signals (Fig. S6).

We then examined the ability of tFCS to measure the distance between two sites in a rigid molecule. To do so, we simulated a rotational diffusion such that the probe dye moved stochastically on the surface of a sphere and at a fixed distance from the reference dye. We found that increasing the distance between the sites gave rise to tFCS signals of increasing amplitude and that these signals were above the noise floor for molecules longer than 18 or 35 nm, depending on the tracking localization accuracy (Fig. S7).

Together, these results show that with a tracking localization accuracy of 100 nm, the theoretical detection limit in tFCS is on the order of 35 nm and that tFCS can measure both distance fluctuations and static distances between two sites at this length scale. Importantly, these simulations highlight how technical limitations affect the spatial resolution and indicate that the spatial resolution could be pushed near the maximal range for fluorescence resonance energy transfer (FRET) ($\sim$ 15 nm) with a smaller tracking localization error.

Measurement of the intramolecular dynamics of DNA

Decades of experimental and theoretical work have led to a deep understanding of the polymer dynamics of double-stranded DNA (dsDNA). Static and dynamical properties of DNA such as radius of gyration, diffusivity, and relaxation timescale have been previously measured using dynamic light scattering (28,29), FCS (30–32), and fluorescence microscopy (33,34). The intramolecular Brownian dynamics of DNA has also been studied by fluorescence microscopy, FCS, and other methods (15,35,36). Here, we used DNA as a benchmark system to experimentally characterize the spatial resolution of our tFCS approach. We labeled dsDNA of 0.5, 1, and 3.9 kbp with a single Cy3b and a single Atto647N at opposite ends (OE) of the molecule. As a control, dsDNA of the same three lengths were labeled with the two dyes placed on the same end (SE) of the duplex, separated by only 31 bp.

We clearly resolved the end-to-end dynamics of both the 1 and 3.9 kbp DNA when we used the side-illumination geometry (Fig. 3 *A*). Conversely, we found that the centered-illumination geometry with near-perfect alignment of the probe and tracking beams resulted in poorer sensitivity and could only resolve the 3.9 kbp DNA (Fig. 3 *B*). The 0.5 kbp DNA fragment was below the resolution threshold for both configurations, as suggested by the overlap of the correlation signal of the SE- and OE-labeled molecules. When observed with the side-illumination geometry, the 3.9 kbp fragments exhibited fluorescence fluctuations with larger correlation amplitude at all time lags and slower timescales of motion compared with the 1 kbp molecules, which was consistent with a larger radius of gyration and slower polymer relaxation modes. Even though the reference and probe sites were nearly colocalized in the SE-labeled DNA molecules, they exhibited a nonzero fluorescence correlation signal (Fig. 3, *A* and *B*), indicating the presence of systematic noise in the tFCS assay. This systematic noise likely stems from imperfect localization of the reference dye, as inferred from our previous simulations (Fig. 2 *F*) and from the triplet-state dynamics of the Atto647N dye, which is also observed in conventional FCS measurements (37,38). Importantly, the assay separates molecules that differ only in the distance between the reference and probe sites (SE and OE constructs) and not in their overall dimensions, indicating that this is an appropriate tool for measuring macromolecular conformation in addition to its ability to measure hydrodynamic properties.

To test the effect of changing the relative position of the reference and probe lasers, which results in a change in the local laser intensity gradient seen by the probe dye, we repeated the measurement with varying tracking-to-probe beam offsets. We found that the changes in the

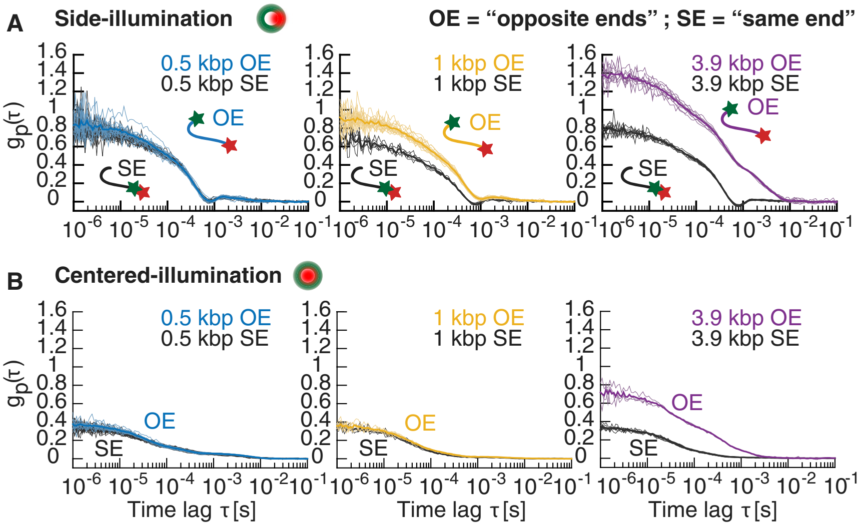

FIGURE 3 tFCS measurement of the end-to-end dynamics of freely diffusing DNA molecules. (*A* and *B*) Fluorescence correlation signals of DNA molecules using the side- (*A*) or centered-illumination (*B*) configuration are shown. DNA were labeled with Cy3b and Atto647N either on opposite ends (OE) or on the same end (SE) of the molecule. DNA lengths were 0.5 kbp (*blue* OE, *black* SE), 1 kbp (*yellow* OE, *black* SE), and 3.9 kbp (*purple* OE, *black* SE). Correlation signals from individual molecules (*thin lines*) and population averages (*thick lines*) are shown. To see this figure in color, go online.

amplitude of the correlation signal and of the mean fluorescence signal had a quadratic dependency in the offset, as predicted analytically (Fig. S8; Supporting Material Appendix Eq. 43). Together, these results demonstrate that the tFCS assay detects the end-to-end dynamics of DNA constructs of ~1 kbp and longer. Based on prior tethered particle motion (39,40) and atomic force microscopy (41) measurements of the RMS distance between the two ends of ~1-kbp-long DNA molecules, these data indicate that we achieved an experimental resolution of 100–150 nm.

Measuring chromatin compaction in freely diffusing molecules

Changes in the local compaction of chromatin regulate multiple essential processes, including gene expression, mitotic chromosome condensation, and heterochromatin formation (42–44). Reconstituted arrays of nucleosomes (45) can recapitulate the mechanics of chromatin condensation in response to electrostatic forces (46,47), chromatin-binding proteins (48), and histone modifications or variants (49). Traditionally, measurements of chromatin compaction in solution use sedimentation assays or analytical ultracentrifugation (AUC) to differentially fractionate compact chromatin (46). However, these assays require a large amount of material and are not typically compatible with complex biochemical systems such as cellular extracts. FRET has been used to study the dynamics of nucleosome arrays but can only probe local conformational changes at the scale of a single nucleosome or a pair of adjacent nucleosomes (50–52). We investigated the applicability of tFCS in characterizing the conformational state of single reconstituted nucleosome arrays and as an alternative approach to studying chromatin structure and dynamics.

We reconstituted nucleosomes on a tandem DNA array of 19 copies of a high-affinity nucleosome-positioning sequence (19×601) (53) labeled with Cy3b and Atto647N on OE. To test whether tFCS could measure changes in the end-to-end distance of individual DNA molecules upon histone assembly, we prepared arrays with increasing histone saturation ratios, defined as the fraction of positioning sites occupied by a histone octamer. Different saturation ratios were obtained by adjusting the relative stoichiometry of histone octamers and positioning sites during assembly, and the ratios were measured at the population level by electrophoresis (Fig. S9 *A*). The amplitude of the side-illumination tFCS signals decreased with the saturation of the arrays, indicating that the assay could detect the reduction in the distance between the two ends of the molecule as a result of DNA wrapping by histones (Fig. 4 *A*). To further quantify the folding state of individual arrays, we computed for each molecule a compaction score quantifying the reduction in amplitude of its correlation signal with respect to the bare 19×601 DNA (Materials and Methods). We found that both the compaction score and the diffusivity of the arrays increased with the histone occupancy level (Figs. 4 *B* and S9, *B* and *C*), confirming that both quantities reflect on the folding state of the molecule. Despite the low concentration of molecules during tracking, the arrays were stable, and it is unlikely that significant nucleosome dissociation occurred during the measurement because the tFCS signals were unchanged even 2 h after dilution of the arrays for tFCS (Fig. S9 *E*).

We next tested whether tFCS could measure the compaction of nucleosome arrays in the presence of divalent cations (46,54). Upon addition of 2 mM $MgCl_2$, we observed a reduction in the tFCS signal amplitude for the 53% saturated arrays along with an increase in diffusivity. For the 6% saturated arrays, neither the tFCS signals nor the diffusion coefficients were significantly affected by the addition of

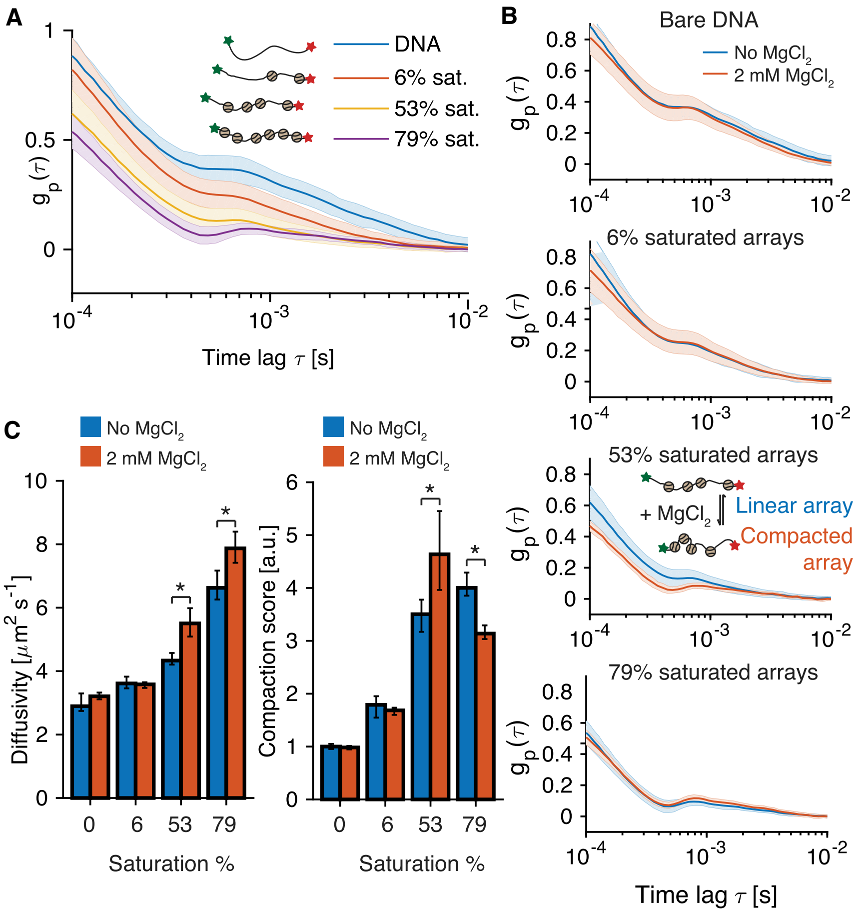

FIGURE 4 Measurement of the compaction state of nucleosome arrays. (*A*) tFCS signals (population median ± standard deviation) for 19×601 DNA molecules before nucleosome assembly (*blue*) and for chromatinized 19×601 molecules with increasing histone occupancy are shown. Data were taken using a side-illumination configuration. (*B*) tFCS measurement of the $MgCl_2$-induced nucleosome arrays compaction is shown as a function of histone occupancy (*top* to *bottom*: bare DNA, 6, 53, and 79% saturated arrays). (*C*) The median (±95% bootstrap confidence intervals) diffusivity (*left*) and compaction score (*right*) of bare DNA and nucleosome arrays before and after addition of 2 mM $MgCl_2$ are shown. The asterisk indicates statistical significance (two-sided Wilcoxon rank sum test, p-value<0.01). To see this figure in color, go online.

magnesium, suggesting that the low nucleosome density in these molecules precludes compaction, which is mediated by intranucleosomal interactions. For the 79% saturated arrays, the addition of 2 mM $MgCl_2$ resulted in a significant increase in their diffusion coefficient, as extracted from the molecule trajectory, indicating that these molecules were able to compact. However, the compaction was not detected in the fluorescence correlation signals. These data can be explained by the fact that the 79% saturated arrays have dimensions on the order of the spatial resolution of the tFCS assay because their diffusion coefficient was close to that of the 1000 bp DNA molecules ($\sim 6-8\ \mu m^2 s^{-1}$), which are the shortest DNA we could resolve. Therefore, further compaction upon magnesium addition cannot be detected. To confirm this hypothesis, we measured the tFCS signals of similarly saturated arrays, but where the probe and reference dye were placed on the SE of the molecule, and we found that indeed the signals of these arrays nearly overlapped with those where the two dyes were on OE of the DNA (Fig. S9 *D*).

Together, these data show that the tFCS approach, when applied within its resolution limits, allows us to measure changes in the compaction of freely diffusing nucleosome arrays at the single-molecule level.

Measurement of repressor-induced DNA-looping dynamics

Control of bacterial operons (55,56), promoter-enhancer interactions in eukaryotes (57), and the large-scale organization of topological domains in metazoan chromosomes (58) are all regulated by chromatin folding to juxtapose DNA sites separated by tens to millions of DNA bases. To demonstrate the ability of tFCS to monitor transient protein-mediated interactions between remote DNA loci, we tested whether we could detect the formation of looped states in freely diffusing DNA induced by lac repressor binding (6,55,59) (Fig. 5).

We generated two 2.6 kbp DNA substrates containing two lac operator sites spaced at specific distances (Table S1): a "looping" construct with the two binding sites at each end of the molecule and a "lasso" construct with one operator site moved to the middle of the molecule (1.3 kbp between the operator sites). For both constructs, we found that addition of lac repressor resulted in the appearance of two populations of molecules characterized by distinct correlation functions (Fig. 5, *C* and *D*). The tFCS signal of the population with the largest correlation amplitude matched the signal measured before the addition of LacI (Fig. 5 *B*),

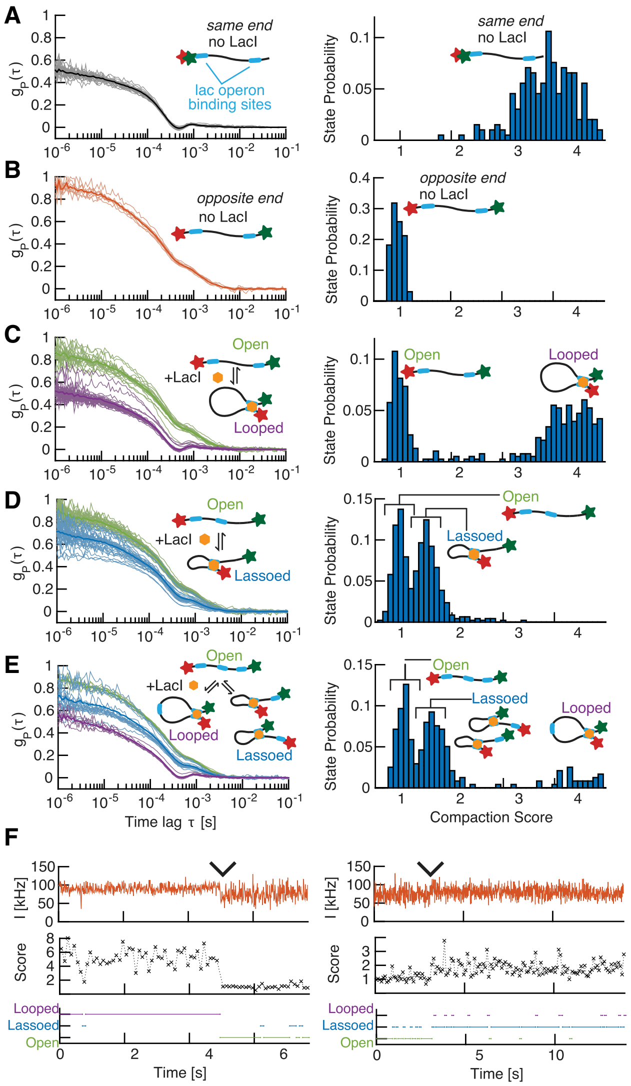

FIGURE 5 Detection of protein-mediated conformational changes. (*A* and *B*) Left: single-molecule tFCS signals (*thin lines*) and population mean (*thick lines*) of the looping DNA construct bearing two lac operators are shown. The molecules were labeled with Atto647N and Cy3b either at the same end (*A*) or on opposite ends (*B*), and data are shown in the absence of LacI. Right: the distribution of compaction scores for the 100 ms subtraces of all the individual molecules is shown. (*C–E*) Left: tFCS signals of individual DNA molecules after addition of 64 nM LacI are shown. The DNA used were the looping construct in (*C*), the lasso construct in (*D*), and the construct with three LacO sites in (*E*). The conformational state inferred by clustering the tFCS signals are categorized as the following: open in green (no LacI bound or LacI bound at a single site), lassoed in blue (LacI-mediated short loop), or looped in purple (LacI-mediated long loop). Cluster averages (*thick lines*) and individual molecules (*thin lines*) are shown for each of these three groups. Right: the distribution of compaction scores for the 100 ms subtraces of all the individual molecules is shown. (*F*) A representative example of a conformational transition between a looped and an open state (*left*) or an open and a lassoed state (*right*), detected during the tracking of an individual molecule. Probe dye fluorescence trace (*top*), 100 ms binned compaction score (*middle*), and inferred conformational state (*bottom*) are shown. Wedges indicate time of transition between the two conformations. To see this figure in color, go online.

which is consistent with molecules in an unlooped conformation (with or without LacI binding). In addition, for the "looping" construct, the tFCS signal of the molecules with the smallest amplitude overlapped with the signal obtained from control DNA molecules in which the two dyes were juxtaposed, validating that these molecules were in a state with the Cy3b and Atto647N dyes in close proximity (Fig. 5 *A*). For the lasso construct, we found that the folded molecules exhibited a signal of intermediate amplitude, which was consistent with the formation of a smaller loop in which the dyes are separated by about half the length of the molecule. Importantly, the addition of 2 mM of the LacI inhibitor isopropyl β-D-thiogalactoside efficiently destabilized the loops (Fig. S10).

To test whether we could distinguish more than two conformational states for a given molecule, we then generated a construct containing three lac operator sites: one at each end of the DNA, as in the looping construct, and one in the middle of the molecule, as in the lasso construct. Because three different pairs of LacO sites can be brought into contact by a LacI tetramer, this construct can adopt four distinct conformational states: 1) an open configuration in which none of the LacO sites are bridged together, 2) a long loop state in which LacI maintains the two terminal LacO sites in contact, 3) a short loop state in which LacI maintains the Cy3b-labeled terminal site in contact with the internal site, and 4) a short loop state in which LacI maintains the Atto647N-labeled terminal site in contact with the internal site. In the presence of LacI, we clearly detected three clusters of tFCS traces. The tFCS signals in the clusters with low, medium, and high amplitudes overlapped with those of the looped molecules from the looping construct, the looped molecules from the lasso construct, and the molecules in the absence of LacI, respectively, indicating that these clusters correspond to the open, short loop, and long loop configurations. However, because the internal site was roughly in the middle of the molecule, we were unable to distinguish between the short loop configurations in 3) and 4), which have almost identical Cy3b-Atto647N distance. Altogether, these measurements demonstrate that the tFCS signal provides a single-molecule readout of the long-range interactions between specific sites, induced by LacI.

Finally, we asked whether we could detect transitions between looped and unlooped states in real time. Because the LacI-mediated loop lifetime (tens of seconds) is long compared with the duration of the tracking traces (6,59), each trace is expected to contain at most one transition. In contrast with the DNA and nucleosome arrays, in which the dynamics is fast (~ 1 ms relaxation timescale) and in which each molecule explores its full conformational space over the course of the measurement, the lac operator/repressor looping dynamics is not at equilibrium during a tracking trace, and it is therefore not meaningful to compute the fluorescence correlation function over the full trace. To scan for the presence of transitions, we segmented each tracking trajectory into 100 ms time bins and computed the fluorescence correlation signal within each bin. We compared the sliding tFCS signal with the average correlation signal of the molecules in the open, folded loop and folded lasso state, and we inferred the state of the molecule at each time point. We inferred transitions between states (looped/unlooped) from changes in the fluorescence fluctuation spectrum across time bins. Representative examples of an unlooping event in the loop construct and a looping event in the lasso construct showed that the transition points uncovered by classifying the 100 ms tFCS signals aligned as expected with abrupt changes in the compaction score and with visible transitions in the amplitude of fluorescence fluctuations (Figs. 5 *F* and S11). These data show that slow conformational dynamics between discrete states can be extracted by segmentation of the tFCS data.

DISCUSSION

A major challenge for studying subcellular biological processes is that few methods can interrogate the structure and dynamics of large macromolecules and complexes at the distance and timescales relevant to their function. We show here that tFCS enables measurement of the internal dynamics of freely diffusing mesoscale molecules in three different experimental systems: DNA molecules in solution, nucleosome arrays, and repressor-protein-induced DNA looping. Because tFCS can be applied to freely diffusing molecules, it is an alternative to trapping-based single-molecule methods to study molecular dynamics in a zero-force regime. The assay is, in its aim, similar to single-molecule FRET, but whereas FRET is powerful for studying fast structural dynamics at the nanometer scale, it cannot be applied to distances greater than ~ 15 nm because of intrinsic limitations in the energy-transfer mechanism (60).

Using DNA of various lengths to benchmark tFCS, we demonstrated that we achieved a spatial resolution of $\sim 100 - 150$ nm. However, this is not a fundamental limit for the technique but the result of practical limitations in the implementation. Even with a 100 nm tracking localization RMS error, our simulations suggest a spatial resolution of ~ 35 nm. Anisotropic tracking accuracy—where the axial particle localization is poorer than the lateral localization, resulting in suboptimal positioning of the molecule within the probe beam—likely accounts for much of the discrepancy between the numerical and experimental resolution. This could be overcome with alternative optical designs, such as using a pair of perpendicularly positioned objectives, which would permit the use of AODs to displace the beam along three directions of space and increase the feedback bandwidth. Imperfect coordination in the motion of the tracking and probe beams may also explain some of the discrepancy, but this could be resolved with improved feedback schemes.

Fundamentally, tFCS spatial and temporal resolutions are limited by photon counting in two ways: 1) the fluorescence intensity of the probe dye determines the level of shot noise in the correlation signal, and 2) the count rate of the tracking dye fluorescence defines the maximal feedback bandwidth that sets the tracking accuracy. tFCS would therefore doubly benefit from brighter and more photostable tags, which are actively being developed (61,62). Such improvements would likely enable the use of tFCS in more complex biochemical environments, such as in cellular extracts. In addition, because tFCS does not require surface immobilization, can track molecules in three dimensions over several tens of micrometers, and operates in a confocal microscopy setting, applications in living cultured cells can be foreseen. The key challenges toward such applications are the development of fluorophores that allow stable imaging of individual molecules within cells with sufficient photon flux and of methods to control the specificity and sparsity of the labeling.

In contrast with traditional localization microscopy techniques, spatial resolution in tFCS is not directly affected by the dimensions of the point spread function but rather by the steepness of the laser intensity gradient at the tracking lock point. This specificity defines an optimization problem for achieving high-resolution imaging, which is distinct from conventional point spread function engineering. It would be interesting to investigate tFCS signals under different excitation profiles, such as those used in light-sheet microscopy (63) or stimulated emission depletion microscopy (64).

The fluorescence fluctuations in tFCS derive from the intramolecular dynamics but also originate from the triplet-state dynamics of the probe dye and from the residual motion of the reference dye in the probe beam frame because of tracking localization error. The convolution of these three processes makes direct fitting of the fluorescence correlation function, as done in conventional FCS, challenging. Future work will focus on deriving methods to better quantify tFCS data. We presented a detailed mathematical analysis of the tFCS signals (Supporting Material Appendix), which suggests that converting the fluorescence correlation into a distance correlation signal to infer the statistics of the relative motion between two sites in calibrated length units is within reach.

We showed that tFCS can measure the Brownian end-to-end dynamics of DNA molecules ranging from 1to4 kbp, but our simulations (Fig. S5) and previous studies indicate that the method can be applied to probe DNA molecules that are several tens of kilobase pairs long (15). Our current experimental resolution is lower than that of tethered particle motion (TPM), which is a standard approach used for studying the time-dependent motion of DNA (6,40). However, tFCS could be done in an immobilized setting with the reference dye tethered to a cover slip, in which case the tracking feedback error would be reduced to zero, and the tFCS resolution would be comparable to the TPM resolution, as suggested by our simulations (Fig. S4). The key advantage of tFCS for the study of biopolymers is that the end-to-end motion can be measured in diffusion and force-free conditions. The volume exclusion effects due to the bead and surface proximity in TPM remain difficult to model and account for and are completely bypassed in tFCS (65). More importantly, the time resolution of TPM is intrinsically limited (~ 1 ms) by the hydrodynamic friction of the bead, which slows down the DNA relaxation and by the camera frame rate (66). Because tFCS is bead-free and the signal is collected by an avalanche photodiode with <1 ns resolution, the time resolution in tFCS is orders of magnitude larger and only limited by the total number of photons collected. tFCS may thus find interesting applications in the measurement of fast DNA relaxation modes, which is important to test polymer models, or in the study of rapid conformational transitions resulting from transient DNA-protein interactions.

Our experiments demonstrate the applicability of tFCS to characterize the compaction state of nucleosome arrays. AUC has been traditionally used to study the response of chromatin to various biochemical perturbations, such as changes in histone composition, salt concentration, or protein activity (46). However, AUC readout is limited to sedimentation coefficients, which are not sufficient to construct precise structural models or characterize the polymer properties of the arrays. Computational studies have proposed different classes of chromatin-fiber structures (67), but we lack experimental measurements to test these models. The end-to-end distance fluctuation spectrum measured by tFCS contains information on the polymer persistence length and relaxation timescales and is amenable to polymer model fitting. We expect that with improved quantification schemes, tFCS of nucleosome arrays will provide a key data set to characterize the polymer properties and structural organization of chromatin under different conditions. Because chromatin organization is thought to regulate genome accessibility and gene expression, we anticipate that tFCS will be impactful in understanding dynamic chromatin processes within the nucleus.

More broadly, tFCS is applicable to probe conformational changes within any large molecular system—such as the macromolecular machines involved in transcription, replication, or chromosome segregation—or within the large elongated proteins implicated in membrane transport. tFCS has the potential to play an important role in the study of these systems, which is similar to the role played by single-molecule FRET in the realm of small individual molecules (<15 nm (68)). We envision that tFCS will be powerfully combined with biochemical manipulations and possibly applied inside living cells to tease apart the basic mechanisms that drive organization at the mesoscale.

SUPPORTING MATERIAL

Supporting Materials and Methods, eleven figures, and two tables are available at http://www.biophysj.org/biophysj/supplemental/S0006-3495(18)30254-6

AUTHOR CONTRIBUTIONS

H.M. and A.F.S. supervised the project. C.L., A.F.S., and H.M. designed the instrumentation and the method. C.L. built the instrument, did the tFCS experiments, and processed the data. C.L., A.F.S., and H.M. designed and interpreted the DNA and chromatin dynamics experiments. C.L., J.C.B., A.F.S., and H.M. designed and interpreted the LacI experiments. C.L. prepared the DNA and nucleosome arrays constructs, J.C.B. purified the lac repressor, and C.J.F. purified the recombinant histones. C.L. developed the analysis pipeline and wrote the code. C.L., J.C.B., A.F.S., and H.M. wrote and/or commented on the manuscript.

ACKNOWLEDGMENTS

We thank Michael Armen for his help with the instrumentation development and his technical assistance, and we thank Andrew Spakowitz, Tom Lampo, Dmitri Pavlichin, and Peter McMahon for insightful discussions on polymer dynamics and stochastic processes. We also thank Dodd Gray for his help with the manuscript; Whitney Johnson, Bradley French, and Frederic Westhorpe for their feedback on the figures; and the members of the Mabuchi and Straight Labs for helpful discussions.

This work was supported by National Institutes of Health grants R01 GM106005 (to A.F.S. and H.M.), R01 GM074728 (to A.F.S.), and by National Science Foundation grant CMMI-0856205 (to H.M.).

REFERENCES

1. Huang, B., M. Bates, and X. Zhuang. 2009. Super-resolution fluorescence microscopy. *Annu. Rev. Biochem.* 78:993–1016.
2. Dekker, J., K. Rippe, …, N. Kleckner. 2002. Capturing chromosome conformation. *Science.* 295:1306–1311.
3. de Wit, E., and W. de Laat. 2012. A decade of 3C technologies: insights into nuclear organization. *Genes Dev.* 26:11–24.
4. Roux, K. J., D. I. Kim, …, B. Burke. 2012. A promiscuous biotin ligase fusion protein identifies proximal and interacting proteins in mammalian cells. *J. Cell Biol.* 196:801–810.
5. Rhee, H. W., P. Zou, …, A. Y. Ting. 2013. Proteomic mapping of mitochondria in living cells via spatially restricted enzymatic tagging. *Science.* 339:1328–1331.
6. Vanzi, F., C. Broggio, …, F. S. Pavone. 2006. Lac repressor hinge flexibility and DNA looping: single molecule kinetics by tethered particle motion. *Nucleic Acids Res.* 34:3409–3420.
7. Han, L., H. G. Garcia, …, R. Phillips. 2009. Concentration and length dependence of DNA looping in transcriptional regulation. *PLoS One.* 4:e5621.
8. Monico, C., A. Tempestini, …, M. Capitanio. 2015. Mapping DNA-LAC repressor interaction with ultra-fast optical tweezer. *2015 Fotonica AEIT Italian Conference on Photonics Technologies.* 1–3.
9. Ha, T. 2014. Single-molecule methods leap ahead. *Nat. Methods.* 11:1015–1018.
10. Berglund, A., and H. Mabuchi. 2005. Tracking-FCS: fluorescence correlation spectroscopy of individual particles. *Opt. Express.* 13:8069–8082.
11. Berglund, A. J., K. McHale, and H. Mabuchi. 2007. Feedback localization of freely diffusing fluorescent particles near the optical shot-noise limit. *Opt. Lett.* 32:145–147.
12. Berglund, A. J., K. McHale, and H. Mabuchi. 2007. Fluctuations in closed-loop fluorescent particle tracking. *Opt. Express.* 15:7752–7773.
13. McHale, K., A. J. Berglund, and H. Mabuchi. 2007. Quantum dot photon statistics measured by three-dimensional particle tracking. *Nano Lett.* 7:3535–3539.

14. McHale, K., and H. Mabuchi. 2010. Intramolecular fluorescence correlation spectroscopy in a feedback tracking microscope. *Biophys. J.* 99:313–322.

15. McHale, K., and H. Mabuchi. 2009. Precise characterization of the conformation fluctuations of freely diffusing DNA: beyond Rouse and Zimm. *J. Am. Chem. Soc.* 131:17901–17907.

16. Cohen, A. E., and W. E. Moerner. 2006. Suppressing Brownian motion of individual biomolecules in solution. *Proc. Natl. Acad. Sci. USA.* 103:4362–4365.

17. Levi, V., Q. Ruan, …, E. Gratton. 2005. Chromatin dynamics in interphase cells revealed by tracking in a two-photon excitation microscope. *Biophys. J.* 89:4275–4285.

18. Katayama, Y., O. Burkacky, …, D. C. Lamb. 2009. Real-time nanomicroscopy via three-dimensional single-particle tracking. *Chemphyschem.* 10:2458–2464.

19. Cardarelli, F., L. Lanzano, and E. Gratton. 2011. Fluorescence correlation spectroscopy of intact nuclear pore complexes. *Biophys. J.* 101:L27–L29.

20. Wang, Q., and W. E. Moerner. 2011. An adaptive anti-Brownian electrokinetic trap with real-time information on single-molecule diffusivity and mobility. *ACS Nano.* 5:5792–5799.

21. Jiang, Y., Q. Wang, …, W. E. Moerner. 2008. Hardware-based anti-Brownian electrokinetic trap (ABEL trap) for single molecules: control loop simulations and application to ATP binding stoichiometry in multi-subunit enzymes. *Proc SPIE Int Soc Opt Eng.* 7038:1–12.

22. Schlau-Cohen, G. S., H. Y. Yang, …, W. E. Moerner. 2015. Single-molecule identification of quenched and unquenched states of LHCII. *J. Phys. Chem. Lett.* 6:860–867.

23. Bockenhauer, S. D., T. M. Duncan, …, M. Börsch. 2014. The regulatory switch of F1-ATPase studied by single-molecule FRET in the ABEL Trap. *In* Proceedings of SPIE 8950, 89500H. International Society for Optical Engineering.

24. Aitken, C. E., R. A. Marshall, and J. D. Puglisi. 2008. An oxygen scavenging system for improvement of dye stability in single-molecule fluorescence experiments. *Biophys. J.* 94:1826–1835.

25. Cordes, T., J. Vogelsang, and P. Tinnefeld. 2009. On the mechanism of Trolox as antiblinking and antibleaching reagent. *J. Am. Chem. Soc.* 131:5018–5019.

26. Guse, A., C. J. Fuller, and A. F. Straight. 2012. A cell-free system for functional centromere and kinetochore assembly. *Nat. Protoc.* 7:1847–1869.

27. Enderlein, J. 2000. Tracking of fluorescent molecules diffusing within membranes. *Appl. Phys. B.* 71:773–777.

28. Sorlie, S. S., and R. Pecora. 1990. A dynamic light scattering study of four DNA restriction fragments. *Macromolecules.* 23:487–497.

29. Smith, D. E., T. T. Perkins, and S. Chu. 1996. Dynamical scaling of DNA diffusion coefficients. *Macromolecules.* 29:1372–1373.

30. Petrov, E. P., T. Ohrt, …, P. Schwille. 2006. Diffusion and segmental dynamics of double-stranded DNA. *Phys. Rev. Lett.* 97:258101.

31. Robertson, R. M., S. Laib, and D. E. Smith. 2006. Diffusion of isolated DNA molecules: dependence on length and topology. *Proc. Natl. Acad. Sci. USA.* 103:7310–7314.

32. Winkler, R. G., S. Keller, and J. O. Rädler. 2006. Intramolecular dynamics of linear macromolecules by fluorescence correlation spectroscopy. *Phys. Rev. E Stat. Nonlin. Soft Matter Phys.* 73:041919.

33. Perkins, T. T., S. R. Quake, …, S. Chu. 1994. Relaxation of a single DNA molecule observed by optical microscopy. *Science.* 264:822–826.

34. Lumma, D., S. Keller, …, J. O. Rädler. 2003. Dynamics of large semiflexible chains probed by fluorescence correlation spectroscopy. *Phys. Rev. Lett.* 90:218301.

35. Shusterman, R., S. Alon, …, O. Krichevsky. 2004. Monomer dynamics in double- and single-stranded DNA polymers. *Phys. Rev. Lett.* 92:048303.

36. Cohen, A. E., and W. E. Moerner. 2007. Principal-components analysis of shape fluctuations of single DNA molecules. *Proc. Natl. Acad. Sci. USA.* 104:12622–12627.

37. Widengren, J., U. Mets, and R. Rigler. 1995. Fluorescence correlation spectroscopy of triplet states in solution: a theoretical and experimental study. *J. Phys. Chem.* 99:13368–13379.

38. Widengren, J., and P. Schwille. 2000. Characterization of photoinduced isomerization and back-isomerization of the cyanine dye Cy5 by fluorescence correlation spectroscopy. *J. Phys. Chem. A.* 104:6416–6428.

39. Nelson, P. C., C. Zurla, …, D. Dunlap. 2006. Tethered particle motion as a diagnostic of DNA tether length. *J. Phys. Chem. B.* 110:17260–17267.

40. Pouget, N., C. Dennis, …, L. Salomé. 2004. Single-particle tracking for DNA tether length monitoring. *Nucleic Acids Res.* 32:e73.

41. Valle, F., M. Favre, …, G. Dietler. 2005. Scaling exponents and probability distributions of DNA end-to-end distance. *Phys. Rev. Lett.* 95:158105.

42. Ho, L., and G. R. Crabtree. 2010. Chromatin remodelling during development. *Nature.* 463:474–484.

43. Chambeyron, S., and W. A. Bickmore. 2004. Chromatin decondensation and nuclear reorganization of the HoxB locus upon induction of transcription. *Genes Dev.* 18:1119–1130.

44. Hübner, M. R., M. A. Eckersley-Maslin, and D. L. Spector. 2013. Chromatin organization and transcriptional regulation. *Curr. Opin. Genet. Dev.* 23:89–95.

45. Hansen, J. C., J. Ausio, …, K. E. van Holde. 1989. Homogeneous reconstituted oligonucleosomes, evidence for salt-dependent folding in the absence of histone H1. *Biochemistry.* 28:9129–9136.

46. Schwarz, P. M., and J. C. Hansen. 1994. Formation and stability of higher order chromatin structures. Contributions of the histone octamer. *J. Biol. Chem.* 269:16284–16289.

47. Schwarz, P. M., A. Felthauser, …, J. C. Hansen. 1996. Reversible oligonucleosome self-association: dependence on divalent cations and core histone tail domains. *Biochemistry.* 35:4009–4015.

48. Georgel, P. T., R. A. Horowitz-Scherer, …, J. C. Hansen. 2003. Chromatin compaction by human MeCP2. Assembly of novel secondary chromatin structures in the absence of DNA methylation. *J. Biol. Chem.* 278:32181–32188.

49. Fan, J. Y., D. Rangasamy, …, D. J. Tremethick. 2004. H2A.Z alters the nucleosome surface to promote HP1α-mediated chromatin fiber folding. *Mol. Cell.* 16:655–661.

50. Torres, T., and M. Levitus. 2007. Measuring conformational dynamics: a new FCS-FRET approach. *J. Phys. Chem. B.* 111:7392–7400.

51. Koopmans, W. J., R. Buning, …, J. van Noort. 2009. spFRET using alternating excitation and FCS reveals progressive DNA unwrapping in nucleosomes. *Biophys. J.* 97:195–204.

52. Poirier, M. G., E. Oh, …, J. Widom. 2009. Dynamics and function of compact nucleosome arrays. *Nat. Struct. Mol. Biol.* 16:938–944.

53. Lowary, P. T., and J. Widom. 1998. New DNA sequence rules for high affinity binding to histone octamer and sequence-directed nucleosome positioning. *J. Mol. Biol.* 276:19–42.

54. Finch, J. T., and A. Klug. 1976. Solenoidal model for superstructure in chromatin. *Proc. Natl. Acad. Sci. USA.* 73:1897–1901.

55. Krämer, H., M. Niemöller, …, B. Müller-Hill. 1987. lac repressor forms loops with linear DNA carrying two suitably spaced lac operators. *EMBO J.* 6:1481–1491.

56. Friedman, A. M., T. O. Fischmann, and T. A. Steitz. 1995. Crystal structure of lac repressor core tetramer and its implications for DNA looping. *Science.* 268:1721–1727.

57. Zhang, Y., C. H. Wong, …, C. L. Wei. 2013. Chromatin connectivity maps reveal dynamic promoter-enhancer long-range associations. *Nature.* 504:306–310.

58. Rao, S. S., M. H. Huntley, …, E. L. Aiden. 2014. A 3D map of the human genome at kilobase resolution reveals principles of chromatin looping. *Cell.* 159:1665–1680.

59. Chen, Y. J., S. Johnson, …, R. Phillips. 2014. Modulation of DNA loop lifetimes by the free energy of loop formation. *Proc. Natl. Acad. Sci. USA.* 111:17396–17401.

60. Krainer, G., A. Hartmann, and M. Schlierf. 2015. farFRET: extending the range in single-molecule FRET experiments beyond 10 nm. *Nano Lett.* 15:5826–5829.

61. Fouz, M. F., K. Mukumoto, …, S. R. Das. 2015. Bright fluorescent nanotags from bottlebrush polymers with DNA-tipped bristles. *ACS Cent. Sci.* 1:431–438.

62. Grimm, J. B., B. P. English, …, L. D. Lavis. 2015. A general method to improve fluorophores for live-cell and single-molecule microscopy. *Nat. Methods.* 12:244–250.

63. Chen, B. C., W. R. Legant, …, E. Betzig. 2014. Lattice light-sheet microscopy: imaging molecules to embryos at high spatiotemporal resolution. *Science.* 346:1257998.

64. Hell, S. W., and J. Wichmann. 1994. Breaking the diffraction resolution limit by stimulated emission: stimulated-emission-depletion fluorescence microscopy. *Opt. Lett.* 19:780–782.

65. Kumar, S., C. Manzo, …, D. Dunlap. 2014. Enhanced tethered-particle motion analysis reveals viscous effects. *Biophys. J.* 106:399–409.

66. Manghi, M., C. Tardin, …, N. Destainville. 2010. Probing DNA conformational changes with high temporal resolution by tethered particle motion. *Phys Biol.* 7:046003.

67. Koslover, E. F., C. J. Fuller, …, A. J. Spakowitz. 2010. Local geometry and elasticity in compact chromatin structure. *Biophys. J.* 99:3941–3950.

68. Roy, R., S. Hohng, and T. Ha. 2008. A practical guide to single-molecule FRET. *Nat. Methods.* 5:507–516.

Biophysical Journal, Volume *114*

Supplemental Information

Measurement of Mesoscale Conformational Dynamics of Freely Diffusing Molecules with Tracking FCS

Charles Limouse, Jason C. Bell, Colin J. Fuller, Aaron F. Straight, and Hideo Mabuchi

Supplementary Materials and Methods

Single molecule tracking microscope: optics

The tFCS microscope was modified from our previously described tracking microscope [1] to increase the feedback bandwidth and permit fast electronic control of the position of both the tracking and probe beams, which is key for the internal dynamics measurements at sub-diffraction limit resolution. For real-time all-optical sensing of the position of the diffusing particle along the X and Y (transverse) axes, we used a 561 nm tracking laser (OBIS diode laser, Coherent Inc.) passing through two acousto-optic deflectors (AODs, 46080-2-LTD, Gooch and Housego) oriented to deflect the beam along the X and Y axes, respectively. The X and Y AODs were driven by 90° phase shifted sine waves so as to move the tracking laser beam around a circular orbit at 100 kHz and generate a particle-position dependent fluorescence modulation. To estimate the position of the particle axially (along the Z axis), we split the tracking laser into two paths corresponding to the s- and p-polarizations, and focused the two beams $\sim$1 µm to 2 µm apart in the sample. Each beam passed through a dedicated acousto-optic modulator (AOM-AF1 IntraAction) that we used as a fast shutter to rapidly (60 kHz) alternate excitation between the s and the p beams, and thereby dither the axial position of the tracking beam focus. The s and p paths were recombined before the X and Y AODs, so that both beams underwent the same rotation in the sample XY plane. To increase the tracking bandwidth and thereby improve the localization accuracy, this core design was updated for faster, photon-counting-limited feedback. The same AODs as the ones used to generate the tracking beam rotation also served as fast actuators allowing for fine adjustments of the beam transverse position with µs scale response time. The relay lenses between the active optical components (AODs) were placed in a 4-f configuration, as standard in confocal scanning systems. The tracking beam partially filled the microscope objective (Zeiss) back aperture to form a focus with a waist of $\sim$500-700 nm in the sample. The sample was mounted on a 3D piezo stage (Nano-PDQ, Mad City Labs). For the 657 nm probe beam, we used a similar optical path with 2 AODs controlling the probe beam position, except that the beam was set-up to form a near diffraction-limited focus (∼320 nm waist) in the sample. The lateral offset between the probe and the tracking lasers was controlled electronically via the probe laser AODs. To facilitate the axial alignment between the tracking and probe beams, we used a tunable lens (el-10-30, Optotune), placed in the path of the probe beam in an infinity space of the microscope. The tunable lens provided us with an electronic knob used in the alignment stage, to easily displace the axial position of the probe beam focus in the sample and position it precisely at the tracking lock point. On the detection side, the fluorescence signal was first separated from the laser light by a dichroic mirror (Chroma ZT405/488/561/640rpc), and then a second dichroic (Chroma 625DCX) separated the probe (Atto647N or Alexa647) and reference (Cy3b) signals. In the reference path, we used a single avalanche photodiode (APD, Perkin-Elmer) to collect individual photons emitted by the Cy3b reference. To record photons from the probe dye, we used either a single APD, or two APDs arranged in a Hanbury Brown Twiss (HBT) configuration to eliminate detection dead time and after-pulsing effects from the fluorescence correlation data. Fluorescence filters were mounted directly in front the reference channel APD (Chroma ET595/50m) and the probe channel APD(s) (Chroma ET705/72m).

Single molecule tracking microscope: feedback

We achieved single-molecule tracking via an analog feedback loop with two feedback branches, which control respectively the position of the piezo stage (slow feedback branch, allowing long range tracking), as well as the position of the tracking laser via the AODs (fast, short range feedback branch). Briefly, the pulses generated by the APD in the reference channels were directly fed into both a dual phase lock-in amplifier (SR830, Stanford Research Systems) phase locked to the (100 kHz) XY rotation of the tracking laser, and into a single-phase lock-in amplifier (SR810, Stanford Research Systems) locked to the (60 kHz) axial dithering. The outputs of the lock-in amplifiers were used as X, Y and Z error signals (lock-in time constant 30 µs for XY, 100 µs for Z) and fed back to the piezo stage driver (Nano Drive, Mad City Labs) via an integral controller. In parallel, the X and Y error signals were fed into a voltage controlled oscillator (VCO) driving the tracking AODs, after band-pass filtering (corner frequencies, 0.3 Hz and 100 Hz) and amplification. The amplification gain was tuned to obtain stable feedback. During tracking, we matched any displacement of the tracking beam with a similar displacement of the probe beam in such a way that both beams tracked the same site on the molecule. To do so, the feedback signal driving the tracking laser VCOs was also applied to the probe laser VCOs after amplification. To calibrate the amplification gain we applied a slow modulation (5 Hz) to the tracking and probe laser VCOs, and monitored the displacements of the beams on a CMOS camera (DCC1645C, Thorlabs). The camera was focused on the back surface of the sample coverslip to image the back reflection of the lasers. We chose a modulation drive that resulted in a ~ 2 µm amplitude modulation of the beam position, and adjusted the relative gain so that both beams followed the same trajectory.

Activation of feedback and fluorescence recording

During the experiments, the stage and the lasers were kept in idle position, but were automatically switched to tracking mode when individual molecules drifted into the confocal illumination volume. Such events were detected by a Schmitt trigger which activated the tracking feedback when the fluorescence of the probe dye was larger than 20-40 kPhotons/s. The feedback remained active until the reference dye bleached or the molecule escaped tracking. The fluorescence signals from the APDs in the reference and probe channels were recorded by a dual-channel time-interval analyzer board (GT653, GuideTech) operating in time-tagged mode, so that the arrival time of each photon was recorded for offline processing. Since we could record from only two APDs at once, the fluorescence signal from the reference dye was not recorded when the HBT configuration was used in the probe channel (the detector configuration used for each experiment is shown in **Table S2**). We will refer to the configuration using a single probe APD as the reference-probe configuration (R-P configuration), and the HBT configuration as the probe-probe configuration (P-P configuration). The tracking laser power was monitored by a Si detector (PDA36A, Thorlabs) placed on a beam pick-off path, and recorded along with the piezo stage position (X, Y and Z channels), with a 10 kHz sampling rate (National Instruments).

Data preprocessing pipeline

To the tFCS signal of individual molecules, the fluorescence and tracking data that were recorded in continuous time were preprocessed by a custom pipeline written in Matlab (Mathworks) consisting of 6 steps, as detailed below.

Step 1: Isolation of individual molecules and fluorescence steps

Periods in the data where the microscope was either in active tracking mode or on standby were first isolated by applying a step detection algorithm to fit the Cy3b fluorescence signal with a piecewise constant signal. To detect abrupt changes, or steps, in the fluorescence mean, we used a simple top-down algorithm, which started with the assumption that there was no step in the fluorescence signal, and added steps one at a time, positioning the new step each time at the location that maximized the likelihood of the data. To decide whether to accept or reject the addition of the new step, we used an f-test to compare the residuals of the two nested models ($n+1$ steps vs n steps). If the p-value of the f-test was larger than a defined threshold, the algorithm stopped and the current segmentation was returned. We adjusted the threshold of the f-test empirically on a test data set, to obtain a qualitatively satisfactory segmentation of the fluorescence signal. The same threshold was used across the different samples to avoid sample bias. To compute the likelihood of the data, we assumed that in between each step, the fluorescence signal was constant with an additive Gaussian noise, where the variance of the noise was equal to the mean signal value (as would be expected for a Poisson emitter). Each interval obtained from the segmentation of the Cy3b signal was further segmented by running the same step finder algorithm on the probe dye signal, in order to isolate sub-intervals where the probe dye was active and sub-intervals where the probe dye was in a dark state. For the experiments where we did not record the tracking dye signal (P-P detector configuration), we applied the segmentation algorithm directly to the probe dye signal of one of the two APDs in the probe channel.

Step 2: Classification of intervals

Segmented intervals were classified into three groups: 0, 1 and 2, representing periods of idle tracking, actively tracked molecules with bleached probe dye, and actively tracked molecules with active probe dye, respectively. To classify the intervals, we generated scatter plots of the probe fluorescence signal, the laser intensity, and either the reference dye fluorescence (R-P configuration) or the laser intensity variance (P-P configuration). The data typically clustered into three groups: low reference fluorescence or tracking laser variance and low probe fluorescence for group 0, high reference fluorescence or tracking laser variance and low probe fluorescence for group 1, high reference fluorescence or tracking laser variance and high probe fluorescence for group 2. Based on the scatter plots, we selected thresholds for the plotted variables that clearly separated the clusters. The thresholds were picked manually, which was the only non-fully automated step in the pipeline.

Step 3: Computation of the raw fluorescence correlation functions and intensities

When both the reference and probe signals were recorded (R-P detector configuration), we computed for each segmented fluorescence period a set of 3 correlation functions: the time auto-correlation of the signal from the reference channel APD $G_r(\tau)$, the auto-correlation of the signal from the probe channel APD $G_p(\tau)$, and the cross-correlation between these two signals $G_{r,p}(\tau)$. These three correlation functions were used to correct for the background signal and estimate the auto-correlation of the fluorescence signal originating from the probe dye only $g_p(\tau)$ (see Background correction section). When the probe signal was recorded from two independent detectors (P-P detector configuration), we computed the cross-correlation between the signals from the two APDs in the probe channel $G_{p/p}(\tau)$. In both cases, the fluorescence correlation functions were computed directly from the time-tagged fluorescence data, consisting of the photon arrival times recorded by each APD, as described elsewhere [2]. The correlation functions were computed at ∼170 values of time-lags, logarithmically spaced between 1 µs and 1 s. For each detector, we also computed the average fluorescence intensity (I_r and I_p in the reference and probe channels, respectively, for the R-P configuration; $I_{p,\mathrm{APD1}}$ and $I_{p,\mathrm{APD2}}$ for the P-P configuration) by dividing the number of photons by the interval duration.

Step 4: Background correction

We modeled the time-dependent signal in the probe channel $I_p(t)$ as the sum of the fluorescence of the probe dye $i_p(t)$, and of a background noise $i_B(t)$. We modeled the background process $i_B(t)$ as the sum of a time-independent Poissonian noise $i_{b,p}$ (which encompasses detector dark noise and scattering from the buffer and the microscope optics), and of a time-dependent crosstalk (or leakage) from the reference dye into the probe channel $i_l(t)$. Likewise, in the reference channel, the measured intensity $I_r(t)$ was modeled as the sum of the fluorescence signal from the reference dye $i_r(t)$ and a background noise $i_{b,r}$. When the crosstalk of the reference dye into the probe channel is negligible, then the measured correlation function in the probe channel $G_p(\tau)$ relates to the true correlation of the probe dye fluorescence (after background correction) $g_p(\tau)$ by an overall time-lag independent rescaling:

$$g_p(\tau) = \frac{1}{\theta_p^2} G_p(\tau) \tag{1}$$

where the background correction factor p is defined as

$$\theta_p = \frac{i_p}{I_p} \tag{2}$$

and where i_p and I_p designate the mean values of $i_p(t)$ and $I_p(t)$, respectively. When the leakage of reference dye into the probe channel is not negligible, the relationship between $G_p(\tau)$ and $g_p(\tau)$ takes a more complicated, time-lag dependent form. In that case, we derived the following expression (SI Appendix):

$$g_p(\tau) = \frac{1}{\theta_p^2} G_p(\tau) + \frac{\theta_l^2(\theta_p - 1)^2}{\theta_p^2 \theta_r^2} G_r(\tau) + \frac{2\theta_l(\theta_p - 1)}{\theta_p^2 \theta_r} G_{r,p}(\tau) \tag{3}$$

where

$$\theta_r = \frac{i_r}{I_r} \qquad \theta_l = \frac{i_l}{i_B} \tag{4}$$

However, we found that the second and third terms in the sum (3) are typically small, and we therefore neglected these terms when data were taken with the P-P configuration of the detectors.

Step 5: Background estimation

To apply the background correction (3, 4), we need to estimate the signal to noise factors θ_r, θ_p and θ_l. This amounts to estimating the mean background scattering intensities $i_{b,r}$, i_b, and the leakage intensity i_l, which may vary from molecule to molecule due to variations in tracking laser power. $i_{b,r}$ and $i_{b,p}$ were first estimated either by doing a blank measurement consisting of recording the fluorescence signal from the buffer in absence of labeled molecules at different tracking laser powers, or equivalently by looking at the intervals in the tFCS data classified in group 0 (**Fig. S1**). For both approaches, we linearly fit the mean noise intensity $i_{b,r/p}$ as a function of the tracking laser power P_{track} to obtain the background scattering coefficients $\alpha_{b,r/p}$ and $\alpha_{b,r/p}$ defined as the coefficients of the linear regression:

$$i_{b,r/p} = \alpha_{b,r/p} P_{\text{track}} + \beta_{b,r/p} \tag{5}$$

To obtain the mean leakage noise, we used the intervals in the data classified in group 1, corresponding to molecules with an active reference dye and bleached probe dye. We estimated the leakage coefficient α as

$$\alpha = \frac{i_l}{i_r} = \frac{\langle I_p - \alpha_{b,p} P_{\text{track}} - \beta_{b,p} \rangle_1}{\langle I_r - \alpha_{b,r} P_{\text{track}} - \beta_{b,r} \rangle_1} \tag{6}$$

where $\langle \rangle_1$ designates the average over molecules in group 1.

Step 6: Optional removal of outliers

For the samples that were expected to be homogeneous (for instance the DNA samples in the end-to-end dynamics measurements) we removed outliers that exhibited a fluorescence correlation function $g_p(\tau)$ distinctively different from the rest of the population. This was achieved by computing for each molecule in group 2 a total variation score calculated as the integral of $g_p(\tau)$ between 1 s and 1 ms, and discarding molecules with a total variation score more that 5 median absolute deviation (MAD) away from the population median.

Estimation of diffusion coefficients

The diffusion coefficient of each molecule was estimated from its trajectory as previously described [3]. Briefly, we computed the mean square displacement of the stage along each axis as a function of the time increment τ, and re-scaled it by dividing by 2τ. The obtained quantity $\hat{D}(\tau)$ provides an estimator of the diffusion coefficient as the function of the time increment, which was fit with a parametric model including the molecule diffusion and the response of the feedback system to obtain the diffusion coefficient of the molecule [3].

Estimation of molecular macrostate in the LacI experiments

In the LacI experiments, we used a clustering algorithm to classify each molecule shown in **Fig. 5B, C, D** as well as the 100 ms subtraces of the molecules shown in **Fig. 5E** as open, looped or lassoed. Clustering was done based on $g_p(\tau)$, using either a two- (lasso and looping construct) or three-components (3 sites construct and 100 ms subtraces) Gaussian Mixture model, representing the distribution of compaction scores and correlation function amplitude (average value of $g_p(\tau)$ between 1-10 μs).

Simulations

For the numerical simulations (**Fig. 2, S4, S5**), we modeled the intramolecular dynamics between the reference and the probe dye as an isotropic 3-dimensional Ornstein-Uhlenbeck (O.U.) process (i.e., the time-autocorrelation of the reference-to-probe dye vector projected along any axis $\sigma rp(\tau)$ is a mono-exponential relaxation $\sigma rp(\tau) = \frac{1}{\sqrt{3}}\sigma_{rp}(0)e^{-\tau/\tau_c}$, where $\sigma_{rp}(0)$ is the RMS amplitude of the reference-to-prove dye motion). We chose a relaxation timescale of $\tau_c = 10\,\mathrm{ms}$ or $\tau_c = 1\,\mathrm{ms}$. To account for localization error during feedback, we modeled the motion of the reference dye with respect to the tracking lock-point as a second, independent O.U. process with a 1 ms relaxation timescale, chosen to match our 1 kHz feedback bandwidth, and an RMS amplitude along each axis of 0, 50 or 100 nm. For each set of parameters, we simulated 20 fluorescence traces of 5 s each. To do so, we first simulated the two O.U. processes using a 1 µs simulation step size to obtain the trajectory of the probe dye position x_p^t with respect to the tracking center. To obtain the probe fluorescence signal, we simulated an inhomogeneous Poisson process with a time-variable instantaneous rate given by

$$i_p(t) = A\Phi\left(x_{\mathrm{err}}^t + x_{r-p}^t - d_{t-p}\right) \tag{7}$$

where d_{t-p} is the tracking-to-probe beam offset, $\Phi(x)$ is the intensity profile of a Gaussian beam with $w(x_z) = w_0\left(1 + \left(\frac{x_z\lambda}{\pi w_0}\right)^2\right)^{1/2}$ describing the axial evolution of the beam waist. The prefactor A was chosen to get an average fluorescence rate of 10^5 photons/s, which is routinely obtained from molecules labeled with a single Atto647N dye (**Table S2**). The Poisson process was simulated using the thinning method [4]. Background scattering noise was simulated separately as an independent Poisson process with a homogeneous rate of 10^4 photons/s, chosen to match the signal-to-noise value of S/N=10 typically observed in our experiments (**Fig. S1**), and added to the probe dye signal. We assessed the resolvability of the intramolecular motion as a function of the reference-to-probe RMS distance by comparing the amplitude of the tFCS signal at short time lags, for which the correlation function has plateaued (either $g_p(\tau = 10\,\mu\text{s})$ or $g_p(\tau = 1\,\mu\text{s})$ for $\tau_c = 10\,\text{ms}$ and $1\,\text{ms}$, respectively) between molecules with a given reference-to-probe RMS distance and control molecules where the probe and reference dyes were co-localized (10 molecules per group, t-test).

DNA preparation and labeling

Each DNA fragment for the DNA dynamics experiment was obtained by digestion of a plasmid with XbaI and EcoRI, followed by gel electrophoresis and gel purification. The plasmids were randomly selected from our database and then screened for their XbaI-EcoRI digestion pattern so as to produce fragments of the desired lengths. The DNA used for the nucleosome arrays assembly was purified by XbaI and EcoRI digestion of a puc18 plasmid containing 19 repeats of the 601 nucleosome positioning sequence, and was the same as the 3.9 kb molecule in **Fig. 3**. To label these molecules, short dsDNAs were prepared by annealing two or three short oligonucleotides, each harboring a specific functionality (XbaI or EcoRI 5‘’ end, Cy3b, Atto647N, or Alexa647 modification), so as to produce appropriate overhangs and fluorescent tags to ligate on the ends of the XbaI-EcoRI fragment for SE or OE labeling (**Table S1**). Ligation was performed by incubation with T4 ligase for 30 min and the ligation products were gel purified. Unmodified oligonucleotides were purchased as used (Integrated DNA Technologies, IDT). Fluorescently labeled oligonucleotides were prepared by conjugation of NHS-Ester reactive dyes (Monoreactive NHS-Ester Cy3b from GE Healthcare, NHS-Ester Atto647N from Sigma, Alexa647 from Invitrogen) to amine-modified oligonucleotides (IDT), followed by PAGE purification.

To prepare DNA constructs containing the LacO sites at desired positions, we designed a GeneBlock (IDT) sequence with two LacO sites separated by ~300 bp which we modified using conventional cloning techniques, to adjust the distance between the two LacO sites, replace the desired LacO sites with shuffled sequences or other LacO variants (LacOsym), or insert a third LacO site in the middle of the construct. Fluorescent labeling of the constructs with Cy3b on one end and Atto647N on the other end was done by PCR amplification with fluorescently labeled primers, followed by gel purification (**Table S1**).

LacI purification

LacI was endogenously expressed from the E. coli BLIM strain (Addgene #35609) transformed with plasmid pLS1 (Addgene #31490). Cultures were grown in 2xYT with 100 ug/mL carbenicillen overnight, and cells were harvested by centrifugation at 4000 x g for 10 minutes. ~36 g of wet cell paste was dounced in 120 mL of Buffer BB (200 mM TrisHCl pH 7.6, 200 mM KCl, 10 mM MgOAc, 2 mM DTT, 5% glucose, 1 mM PMSF and 0.25 mg/mL lysozyme) then flash frozen and stored at -20 C. Phosphocellulose was prepared by swelling 20 g of phosphocellulose in 1 L of water, then decanted. This process was repeated (in 1L volumes): 3X water, 4X 0.5 N NaOH, 1X water, 4X 0.5 N HCl, 1X water, and 2X 0.2 M KHPO4 (pH 7.6). The slurry was transferred to a Buchner funnel with a porous ceramic filter and washed with 0.2 M KHPO4 (pH 7.6). The slurry was then poured into a column packed by gravity flow with a final bed volume of ~120 mL. The frozen cell slurry was thawed at 4C and stirred in a beaker for 20-30 minutes. The lysate was then treated with 2 mg of DNase and stirred for 5-10 minutes. The lysate was dounced, then centrifuged at 12k rpm in a JA 20 rotor for 40 minutes. The supernatant was transferred to a beaker, and ammonium sulfate was slowly added while stirring to a final concentration of 23.1 g AmSO4 per 100 mL lysate. The precipitated lysate was centrifuged for 10 minutes at 4000 x g, and the pellet was resuspended in Buffer BB plus 23.1 g/mL AmSO4, dounced and centrifuged again. The pellet was then resuspended in 40 mL of Buffer A (45 mM KHPO4 (pH 7.6), 5% glucose and 1 mM DTT) and then dialyzed overnight against 2L of the same buffer. The lysate was centrifuged at 4000 g for 15 minutes to remove insoluble material, and then loaded onto the phosophocellulose column equilibrated in Buffer A. After the lysate was loaded, the column was washed with Buffer A until the UV absorbance returned to baseline. A linear gradient was run over 120 minutes with a flow rate of 0.8 mL/mL from Buffer A to Buffer B (300 mM KHPO4 (pH 7.6), 5% glucose and 1 mM DTT). Fractions were collected and UV absorbance was monitored. The major peak fractions (~38 mL) were pooled containing ~50 mg of >90% pure LacI, which was then concentrated via precipitation by adding 8.8 g AmSO4, centrifuging at 8000 rpm in a JA 20 rotor for 20 minutes. The LacI pellet was resuspended in 4.5 mL Buffer B, and injected into a S200 HiLoad 16/60 size exclusion column equilibrated with Buffer B. ~10% of the input protein eluted in the void volume and was discarded, with the remaining protein eluting as a homogeneous peak consistent with the column mobility of a tetramer. Peak containing fractions were pooled and flash frozen. The concentration was determined using an extinction coefficient of $22\,450\,\mathrm{M^{-1}\,cm^{-1}}$ (monomer) and determined to be free of DNA contamination (260/280 ratio = 0.45).

Nucleosome arrays reconstitution

To reconstitute nucleosome arrays [5], we prepared individual 20 µL assembly mixes each containing unlabeled 19x601 DNA (19-mer tandem array of the 601 positioning sequence) at a concentration of 1.5 µM of 601 monomers, dual-labeled 19x601 DNA (with a single Cy3b and a single Atto647N placed either on the same end or on opposite ends of the DNA) at 150 nM of 601 monomers and variable amounts of purified H3/H4/H2A/H2B octamers in high salt buffer (HSB: 10 mM Tris pH 7.4, 0.1 mM EDTA, 2M NaCl). Unlabeled DNA was used in addition to labeled DNA at a 10:1 ratio to increase the overall array concentration during tFCS and thus minimize histone dissociation, while maintaining the concentration of labeled molecules at $\sim 1\,\mathrm{pM}$). Additionally, a 0.5x excess of H2A/H2B dimers per 601 monomer was added to each assembly to increase the array stability against dimer exchange. We used individual mixes to titrate the stoichiometric ratio of octamers from 0.4 to 1.4 per

601 site. Each assembly mix was loaded into a 20 µL dialysis button (Hampton Research) sealed with a 3.5 kDa MWCO dialysis membrane (Spectrum Labs). The buttons were plunged into 500 mL of HSB, which was slowly exchanged using a system of peristaltic pumps against 2 L of low salt buffer (LSB: 10 mM Tris pH 7.4, 0.1 mM EDTA, 10 mM NaCl), over 36 hours (0.5 mL/minute). The quality of each array assembly was assessed by AvaI restriction digest (overnight incubation at room temperature) followed by native-PAGE electrophoresis [5]. AvaI cuts in between each monomeric repeat of the positioning sequence and allows us to determine the histone saturation ratio (average fraction of 601 sites occupied by a histone octamer).

Appendix: Mathematical derivations

Background correction of fluorescence correlation functions

We model the signal in the reference channel I_r^t (where the exponent t indicates the time dependency of the signal) as the sum of the fluorescence signal from the reference dye i_r^t and a constant background scattering $i_{b,r}$. The signals I_r^t and i_r^t refer to the instantaneous photon emission rates, and are stochastic processes driven by the random trajectory of the probe dye within the probe beam. In the probe channel, we model the measured signal I_p^t as the sum of the probe dye fluorescence signal i_p^t, a constant background scattering $i_{b,p}$, and a leakage intensity $i_l^t = \alpha i_r^t$, where α is the leakage coefficient accounting for the fluorescence crosstalk between the reference and probe channels.

The measured instantaneous intensities in the reference and probe channels are therefore:

$$I_r^t = i_r^t + i_{b,r} \tag{8}$$

$$I_p^t = i_p^t + i_B^t \tag{9}$$

where the total background in the probe channel is

$$i_B^t = \alpha i_r^t + i_{b,p} \tag{10}$$

We define the signal-to-noise ratios

$$\theta_r = \frac{i_r}{I_r} \qquad \theta_p = \frac{i_p}{I_p} \qquad \theta_l = \frac{i_B - i_{b,p}}{i_B} \tag{11}$$

where we dropped the t subscript to indicate time-averaged intensities.

The cross-correlation between two generic stationary stochastic signals a^t and b^t with mean values a and b is defined as

$$\begin{align} g[a,b](\tau) &= \frac{\mathbb{E}\left[a^t b^{t+\tau}\right]}{\mathbb{E}\left[a^t\right]\mathbb{E}\left[b^t\right]} - 1 \tag{12} \\ &= \frac{\mathbb{E}\left[a^t b^{t+\tau}\right]}{ab} - 1 \tag{13} \end{align}$$

and the auto-correlation of a^t is simply denoted

$$g[a](\tau) = \frac{\mathbb{E}\left[a^t a^{t+\tau}\right]}{a^2} - 1 \tag{14}$$

To express the auto-correlations of the reference and probe dye fluorescence intensities $g_r(\tau)$ and $g_p(\tau)$ (as a short-hand notation for $g[i_r](\tau)$ and $g[i_p](\tau)$) and their cross-correlation $g_{r,p}(\tau)$ (as a short-hand notation for $g[i_r, i_t](\tau)$), as a function of the auto-correlations and the cross-correlations of the measured signals $G_r(\tau)$, $G_p(\tau)$ and $G_{r,p}(\tau)$ (as a short-hand notation for $g[I_r](\tau)$, $g[I_p](\tau)$ and $g[I_r, I_p](\tau)$, respectively), we use Eq. 8 and the following algebraic relationship on correlation functions, which is valid for any stochastic stationary signal a_t, b_t, c_t, d_t :

$$g[a+b, c+d] = \frac{a}{a+b}\frac{c}{c+d}g[a,c] + \frac{a}{a+b}\frac{d}{c+d}g[a,d] + \frac{b}{a+b}\frac{c}{c+d}g[b,c] + \frac{b}{a+b}\frac{d}{c+d}g[b,d] \tag{15}$$

We find that the measured ($G(\tau)$) and background-corrected ($g(\tau)$) correlation functions are related by the linear transformation:

$$\begin{bmatrix} G_r \\ G_p \\ G_{r,p} \end{bmatrix} = \begin{bmatrix} \theta_r^2 & 0 & 0 \\ (1-\theta_p)^2\theta_l^2 & \theta_p^2 & 2\theta_p(1-\theta_p)\theta_l \\ \theta_r(1-\theta_p)\theta_l & 0 & \theta_r\theta_p \end{bmatrix} \begin{bmatrix} g_r \\ g_p \\ g_{r,p} \end{bmatrix} \tag{16}$$

This derivation uses the fact that the scattering background $i_{b,p}$ (resp. $i_{b,r}$) and the fluorescence signal i_p^t (resp. i_r^t) in the probe (resp. reference) channel are statistically independent, so the cross-correlation between these two processes vanishes.

We can finally invert this relation to get:

$$\begin{bmatrix} g_r \\ g_p \\ g_{r,p} \end{bmatrix} = M \begin{bmatrix} G_r \\ G_p \\ G_{r,p} \end{bmatrix} \tag{17}$$

where

$$M = \begin{bmatrix} \frac{1}{\theta_r^2} & 0 & 0 \\ \frac{\theta_l^2(\theta_p-1)^2}{\theta_p^2\theta_r^2} & \frac{1}{\theta_p^2} & \frac{2\theta_l(\theta_p-1)}{\theta_p^2\theta_r} \\ \frac{\theta_l(\theta_p-1)}{\theta_p\theta_r^2} & 0 & \frac{1}{\theta_p\theta_r} \end{bmatrix} \tag{18}$$

which shows that we can obtain the background corrected correlation function of the probe dye signal $g_p(\tau)$ from the measured auto-correlations of the signals recorded in the probe and reference channels and their cross-correlation.

Relationship between the fluorescence correlation signal in tFCS and the motion of the probe dye

In this section, we describe the mathematical formalism necessary to analyze the tFCS signals. We describe some assumptions which allow us to obtain a tractable form for the fluorescence correlation function $g_p(\tau)$, which is useful to gain insight into the relationship between the intramolecular dynamics and the fluorescence correlation signal.

General expression of the fluorescence correlation signal in tFCS

In absence of dye blinking, the probe fluorescence is described by a Poisson process with time-varying intensity i_p^t

$$i_p^t = P\eta\phi(x_p^t - d) \tag{19}$$

where P is the laser power, η is the quantum yield of the dye, $\phi(x)$ is the spatial distribution of the probe beam intensity, x_p^t is the position of the probe dye (vector of dimension 3 representing the x,y and z coordinates with respect to the center of the tracking beam), and d is the offset vector between the tracking and probe beams. To account for the photophysics of the dye, we describe the dye intrinsic dynamics with a stochastic process D^t.

An important assumption is that the dye dynamics is independent of the motion of the dye in the beam. Under this assumption, the fluorescence intensity from the probe can be written as

$$\tilde{i}_p^t = D^t i_p^t \tag{20}$$

and the fluorescence autocorrelation of the probe dye fluorescence is, using the notations defined in Eq. 12

$$g[\tilde{i}_p](\tau) = -1 + (1 + g[D](\tau))\,(1 + g[i_p](\tau)) \tag{21}$$

Therefore, given the illumination profile $\phi(x)$, if one has a parametric model for the blinking dynamics of the dye D^t and for the statistics of the probe dye motion x_p^t, one can use Eqs.

19 and 21 to derive an expression for the fluorescence autocorrelation and use parametric estimation techniques to fit the experimental correlation data. In the next section, we show that if the probe dye motion x_p^t satisfies some conditions, then an analytical expression can be derived for $g[i_p]$.

Simplified form of the fluorescence correlation signal in tFCS in the case of a Gaussian process

The fluorescence correlation function of an individual molecule in tFCS under these conditions was derived previously [6]. Here, we derive the expression of the fluorescence correlation in the case of a variable offset between the tracking and probe beams. We show that the amplitude of the fluorescence correlation function has, upon renormalization, a quadratic dependency in the value of the tracking-to-probe beam offset. To derive an analytic expression for $g[i_p]$, we make the following assumptions:

1. The intensity profile of the probe beam is described by a 3-dimensional Gaussian: $\phi(x) = e^{-2w^{-T}xw^{-1}}$ where w is a 3x3 diagonal matrix with the beam waist along the three axes (w_x, w_y and w_z) as entries.

2. The process x_p^t is a stationary Gaussian process, in the sense where it is fully described by its second order statistics (for a more precise definition, see [7]).

$$\sigma_p(\tau) = \mathbb{E}\left[x_p^t(x_p^{t+\tau})^T\right] \tag{22}$$

3. The blinking dynamics of the probe dye is independent of the tracking-to-probe beam offset d.

Under these assumptions, the fluorescence correlation function can be computed analytically. We first normalize all of the length variables with respect to the beam dimensions by defining:

$$X_p^t = 2w^{-1}x_p^t \quad , \quad \delta = 2w^{-1}d \tag{23}$$

For computational purposes, we also define the two-timepoint vectors Y and Δ (expressed in block matrix notations):

$$Y = \begin{bmatrix} X_p^t \\ X_p^{t+\tau} \end{bmatrix} \qquad \Delta = \begin{bmatrix} \delta \\ \delta \end{bmatrix} \tag{24}$$

Under assumption 2, the statistics of Y are entirely defined by the covariance matrix

$$\Sigma(\tau) = \mathbb{E}\left[YY^T\right] \tag{25}$$

which itself relates to the covariance matrix of the probe dye motion $\sigma_p(\tau)$ (Eq. 22) by the expression (in block matrix notation)

$$\Sigma(\tau) = 4W^{-1} \begin{bmatrix} \sigma_p(0) & \sigma_p(\tau) \\ \sigma_p(\tau) & \sigma_p(0) \end{bmatrix} W^{-1} \tag{26}$$

where

$$W = \begin{bmatrix} w & 0 \\ 0 & w \end{bmatrix} \tag{27}$$

(W is a 6x6 matrix, written above in block notations). By writing

$$i_p(t)i_p(t+\tau) = e^{-\frac{1}{2}(Y-\Delta)^T(Y-\Delta)}$$

and by using the probability density for a Gaussian process

$$\mathbb{P}[\phi(Y) = y] = \frac{1}{\sqrt{(2\pi)^6 \det(\Sigma)}} e^{-\frac{1}{2}(y-\Delta)^T\Sigma^{-1}(y-\Delta)} \tag{28}$$

we obtain the autocorrelation of the intensity :

$$\mathbb{E}\left[i_p(t)i_p(t+\tau)\right] = \frac{1}{\sqrt{\det(\mathbf{1}+\Sigma)}} e^{-\frac{1}{2}\Delta^T\left(\mathbf{1}-\Sigma(\mathbf{1}+\Sigma)^{-1}\right)\Delta} \tag{29}$$

Likewise, the expectation value for the intensity is

$$\mathbb{E}\left[i_p(t)\right]\mathbb{E}\left[i_p(t+\tau)\right] = \frac{1}{\sqrt{\det(\mathbf{1}+\Sigma_\infty)}} e^{-\frac{1}{2}\Delta^T\left(\mathbf{1}-\Sigma_\infty(\mathbf{1}+\Sigma_\infty)^{-1}\right)\Delta} \tag{30}$$

where

$$\Sigma_\infty = 4W^{-1}\begin{bmatrix}\sigma(0) & 0 \\ 0 & \sigma(0)\end{bmatrix}W^{-1} \tag{31}$$

We finally get the expression for the fluorescence correlation function

$$g[i_p](\tau) = \frac{\sqrt{\det(\mathbf{1}+\Sigma_\infty)}}{\sqrt{\det(\mathbf{1}+\Sigma)}} e^{-\frac{1}{2}\Delta^T\left(\Sigma_\infty(\mathbf{1}+\Sigma_\infty)^{-1}-\Sigma(\mathbf{1}+\Sigma)^{-1}\right)\Delta} - 1 \tag{32}$$

This expression assumes that the coordinate system is such that $E[x_p^t] = 0$, which can always be obtained modulo a redefinition of the tracking-to-probe-beam offset d.

Fluorescence correlation signal in tFCS for an isotropic process with independent axes

Under the assumption that the motion is isotropic and there is no cross-correlation between the x, y, z axes (this excludes a rigid body rotation, because in that case the motion along the 3 axes is correlated), we can further simplify Eq. 32. The process $x_p(t)$ is then fully characterized by the length correlation (in space units) $s_0 s(\tau) = \mathbf{E}\left[x_p(t)^T x_p(t+\tau)\right]$ where $s(\tau)$ is normalized so that $s(0) = 1$, and we can write Σ as

$$\Sigma = s_0 W^{-2} + s_0 s(\tau) W^{-1} K W^{-1} \tag{33}$$

where

$$K = \begin{pmatrix} 0 & \mathbf{1}_3 \\ \mathbf{1}_3 & 0 \end{pmatrix} \tag{34}$$

If we assume that the illumination is isotropic along the x and y axis, we can define $w_{\parallel} = w_x = w_y =$ and $\epsilon = \frac{w_{\parallel}}{w_z}$. Then we obtain

$$1 + g_p(\tau) = \frac{(1+v)^2}{(1+v+s(\tau)v)(1+v-s(\tau)v)} \frac{1+\epsilon v}{\sqrt{(1+\epsilon v+s(\tau)\epsilon v)(1+\epsilon v-s(\tau)\epsilon v)}} \\ \exp\left(\frac{d_{\parallel}^2 s(\tau)v}{(1+v)(1+v+s(\tau)v)} + \frac{\epsilon^2 d_{\perp}^2 s(\tau)\epsilon v}{(1+\epsilon v)(1+\epsilon v+\epsilon s(\tau)v)}\right) \tag{35}$$

where $v = \frac{4}{3}s_0/w_{\parallel}^2$ is the mean square amplitude of the probe motion normalized with respect to the beam size. Note that in the case where the probe dye motion is described by an Ornstein-Uhlenbeck process with relaxation timescale τ_c, as it is the case in our simulations (**Fig. 2, S5, S7**), the normalized length cross-correlation is $s(\tau) = e^{-\tau/\tau_c}$.

Effect of the tracking localization error

The presence of tracking error is straightforward to take into account. Denoting x_r^t the position of the reference dye with respect to the center of the tracking beam rotation, we can express the probe dye position x_p^t as the sum of a vector describing the intramolecular dynamics $x_{\text{r-p}}^t = x_p^t - x_r^t$ (i.e. the reference-to-probe dye dynamics) and of a vector describing the tracking error $x_{\text{err}}^t = x_r^t$ (which is equal to zero in the case of perfect tracking),

$$x_p^t = x_{\text{r-p}}^t + x_{\text{err}}^t \tag{36}$$

Since the molecular dynamics and the tracking error are statistically independent, the covariance matrix has the form

$$\Sigma(\tau) = \Sigma_{\text{r-p}}(\tau) + \Sigma_{\text{err}}(\tau) \tag{37}$$

and the correlation function is now, using Eq. 32

$$g[i_p](\tau) = -\mathbf{1} + \sqrt{\frac{\det\left(\mathbf{1} + \Sigma_{\text{r-p},\infty} + \Sigma_{\text{err},\infty}\right)}{\det\left(\mathbf{1} + \Sigma_{\text{r-p}} + \Sigma_{\text{err}}\right)}} \\ e^{-\frac{1}{2}\Delta^T\left((\Sigma_{\text{r-p},\infty}+\Sigma_{\text{err},\infty})(\mathbf{1}+(\Sigma_{\text{r-p},\infty}+\Sigma_{\text{err},\infty}))^{-1}-(\Sigma_{\text{r-p}}+\Sigma_{\text{err}})(\mathbf{1}+(\Sigma_{\text{r-p}}+\Sigma_{\text{err}}))^{-1}\right)\Delta} - 1 \quad (38)$$

Note that the contributions from the tracking error and the end-to-end motion do not factorize, and we cannot write the correlation function as a product of an internal dynamics part and a tracking error part.

Relative correlation function

In order to compare the fluorescence correlation functions in the centered- and side-illumination conditions, we define the relative fluorescence correlation function as:

$$g_{\text{rel}}[\tilde{i}_b](\tau) = \ln\left(1 + g[\tilde{i}_p](\tau, \delta = \delta_1 c)\right) \quad (39)$$

$$- \ln\left(1 + g[\tilde{i}_p](\tau, \delta = \delta_2 c)\right) \quad (40)$$

$$= g_{\text{rel}}[D](\tau) + g_{\text{rel}}[i_p](\tau) \quad (41)$$

where c is the unit vector along which the probe beam is being displaced with respect to the tracking beam, δ_1 and δ_2 are scalar values of the offset in the centered- and side-illumination condition, respectively (typically $\delta_1 = 0$). We also define the relative intensity:

$$\tilde{i}_{\text{rel}} = 2\ln\left(\frac{\tilde{i}_b[\delta = \delta_1 c]}{\tilde{i}_b[\delta = \delta_2 c]}\right) \quad (42)$$

Under assumption 3, the term corresponding to the dye dynamics $g_{\text{rel}}[D]$ in Eq. 41 vanishes and we obtain

$$g_{\text{rel}}[\tilde{i}_b](\tau) = (\delta_2^2 - \delta_1^2)\frac{1}{2}C^T\left(\Sigma_\infty(\mathbf{1} + \Sigma_\infty)^{-1} - \Sigma(\mathbf{1} + \Sigma)^{-1}\right)C \quad (43)$$

where $C = \begin{bmatrix} c \\ c \end{bmatrix}$. Likewise, the relative intensity becomes

$$i_{\mathrm{rel}} = (\delta_2^2 - \delta_1^2)\frac{1}{2}C^T\left(\mathbf{1} - \Sigma_\infty(\mathbf{1} + \Sigma_\infty)^{-1}\right)C \tag{44}$$

This expression shows that the relative correlation function and the relative intensity have a quadratic dependency in the offset amplitude δ_2, which we verified experimentally in **Fig. S8**.

References

[1] McHale, K., Berglund, A. J. & Mabuchi, H. Quantum dot photon statistics measured by three-dimensional particle tracking. *Nano letters* **7**, 3535–9 (2007).

[2] Laurence, T. A., Fore, S. & Huser, T. Fast, flexible algorithm for calculating photon correlations. *Optics letters* **31**, 829–31 (2006).

[3] McHale, K. & Mabuchi, H. Precise characterization of the conformation fluctuations of freely diffusing DNA: beyond Rouse and Zimm. *Journal of the American Chemical Society* **131**, 17901–7 (2009).

[4] Lewis, P. A. W. & Shedler, G. S. Simulation of nonhomogenous Poisson processes by thinning. *Naval Research Logistic Quarterly* **26**, 403–414 (1979).

[5] Guse, A., Fuller, C. J. & Straight, A. F. A cell-free system for functional centromere and kinetochore assembly. *Nature protocols* **7**, 1847–69 (2012).

[6] McHale, K. & Mabuchi, H. Intramolecular fluorescence correlation spectroscopy in a feedback tracking microscope. *Biophysical journal* **99**, 313–22 (2010).

[7] MacKay, D. J. C. *Information theory, inference and learning algorithms. Cambridge University Press* (2003).

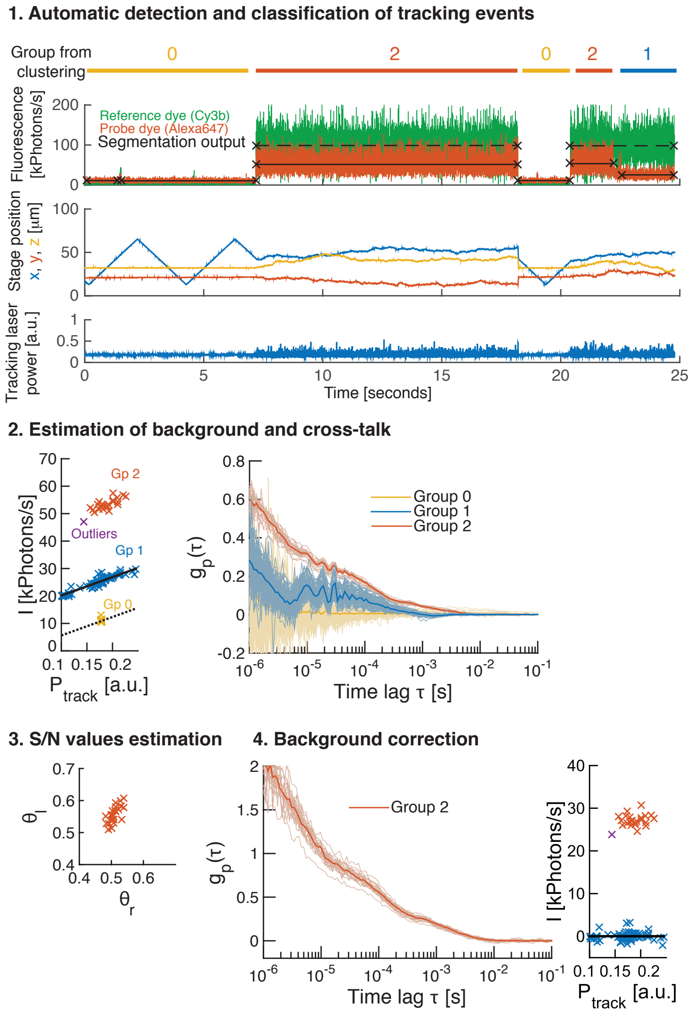
1. Automatic detection and classification of tracking events

2. Estimation of background and cross-talk

3. S/N values estimation

4. Background correction

Figure S1. Data pre-processing pipeline: detection of individual molecules and background correction All data shown are from the 3.8 kbp OE DNA molecules (**Fig.** 3) and were recorded using the side-illumination.

***Step 1**: Detection and classification of time intervals in the recorded data corresponding to individual molecules.* Typical time course of the probe fluorescence signal (top plot, binned at 3 ms for visualization), the microscope stage position (middle plot), and the tracking laser power (bottom plot) during a tFCS experiment. Individual molecules spontaneously drift in the confocal detection volume (e.g.: $t = 7 - 17$ s) and trigger activation of the feedback loop. This is observed in the abrupt change in laser power, which is adjusted in real-time to maintain the probe dye fluorescence signal constant, the transition in the stage signal from an idle stage (except along the X-axis, which is programmed to scan the sample during stand-by mode to reduce the dwell time between two tracking events) to a stochastic Brownian trajectory, and the increase in probe dye fluorescence. The probe dye of an individual molecule can either bleach before the reference dye, in which case the molecule is still tracked but the probe fluorescence signal displays a single step drop (e.g. $t \sim 22\,\mathrm{s}$), or can stay active till the molecule escapes tracking (e.g., $t \sim 17\,\mathrm{s}$), for instance due to bleaching of the reference dye. Top line shows the outcome of the clustering step, which classifies time periods corresponding to: periods of idle tracking (group 0), actively tracked molecules with a bleached probe dye (group 1), or actively tracked molecules with an active probe dye (group 2). The segmentation of the continuous data into time periods is done automatically by a step finder algorithm applied to the tracking and probe dye florescence signals, the output of which is shown as black lines overlaid on the florescence traces (step finder applied to the reference and probe dye signal shown as dashed and plain line, respectively). ***Step 2**: Estimation of background (scattering and leakage from the reference dye into the probe channel) as a function of the tracking laser power.* Left: Scatter plots of the probe fluorescence intensity and the tracking laser power during individual fluorescence periods. Groups 0 and 1 are used to estimate the background scattering noise as a function of laser power (dashed line), as well as the total background in the probe channel which includes scattering noise and fluorescence leakage of the tracking dye into the probe channel (plain line). Right: time autocorrelation function of the fluorescence intensity in the probe channel for individual fluorescence periods (thin lines), color coded by group. Group averages are shown as thick lines. Group 0 events exhibit a flat correlation signal confirming that these periods do not correspond to background noise. Group 1 molecules exhibit a non-flat correlation signal, which reports on the leakage of reference dye (the only active dye for this group) into the probe channel. Oscillations at short time lag are visible and stem from the 100 kHz rotation of the tracking laser. ***Step 3**. Estimation of signal-to-noise values.* Scatter plot of the signal-to-noise factors θ_l and θ_r estimated for each molecule in group 2. ***Step 4**. Background corrected fluorescence intensities and correlation functions.* Left: Fluorescence correlation functions of individual molecules in group 2, after background correction, applied using the signal-to-noise factors evaluated in Step 3. Right: Same scatter plot as in step 2, but after background correction.

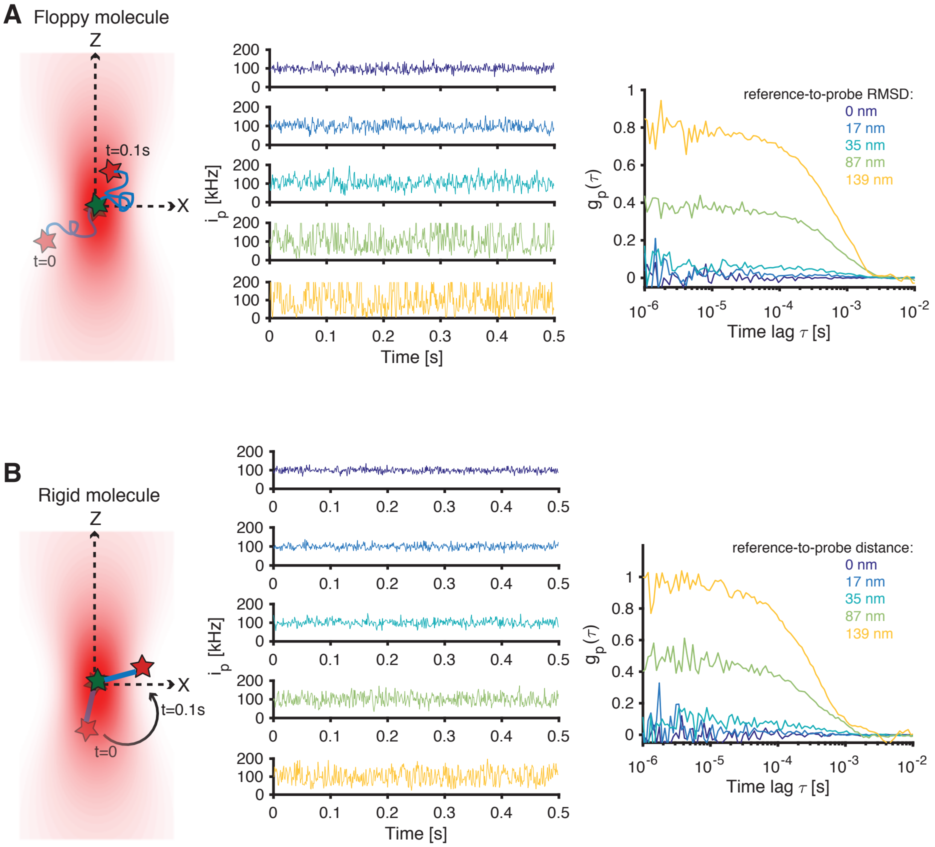

Figure S2. Readout of intramolecular distances in tFCS. Schematic of the molecular motion that generates fluorescence fluctuations and simulated tFCS data for (A) floppy molecules and (B) rigid molecules with a fixed distance between the reference and probe dyes. In both (A) and (B), the probe intensity trace $i_p(t)$ (middle panel) and the corresponding fluorescence correlation function $g_p(\tau)$ (right panel) are shown for individual molecules of various lengths. For floppy molecules, where the distance between the reference and probe dyes fluctuates, the amplitude of the intensity fluctuations and of the correlation signal encode the reference-to-probe dye root mean square distance (RMSD). For rigid molecules, the intensity fluctuations result from the rotational diffusion of the molecule about the reference dye and thus directly encode the reference-to-probe dye distance. The dynamics model used in (A) and (B) is the same as in **Fig. S4** and **Fig. S7**, respectively. Each molecule was simulated for 5 s, with 500 000 photons collected (100 000 photons/s mean fluorescence rate) and using a side-illumination geometry (probe beam waist $w = 310\,\text{nm}$, probe beam offset $1.0\,w$ in (A) and $1.2\,w$ in (B)).

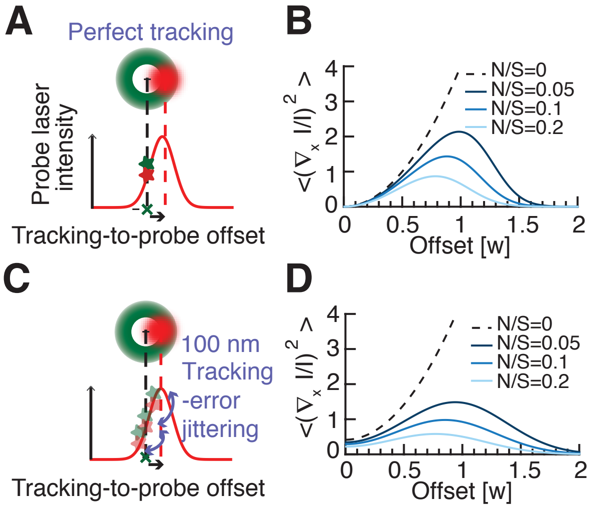

Figure S3. Heuristic spatial sensitivity of the tFCS assay. (**A**) Schematic representation of the side-illumination configuration, with tunable tracking-to-probe beam offset (same as in **Fig. 2**) (**B**) Curves show the relative intensity gradient as a function of the tracking-to-probe beam offset (in units of beam waist w) for various noise-to-signal N/S values (N is the background intensity and S is the fluorescence intensity from the probe dye placed at the focus of the beam, typical experimental value $N/S \sim 0.2$). (**C,D**) Same as in (A,B) but taking into account imperfect feedback (100 nm RMS localization error) which results in a jittering of the reference dye in the illumination profile. The jittering effectively reduces the probe laser intensity gradient seen by the probe dye.

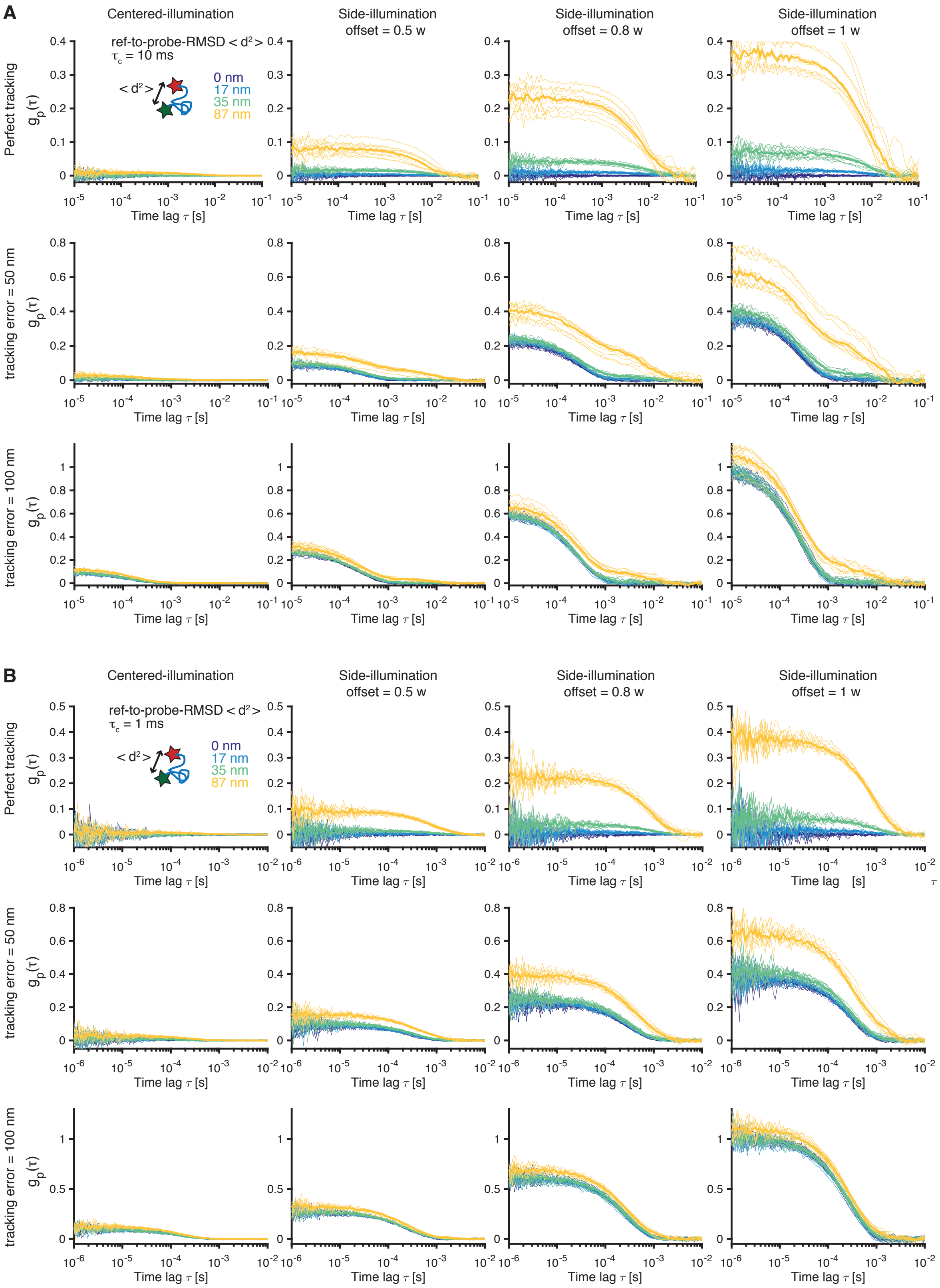

Figure S4. Spatial resolution of tFCS - numerical simulations.

Simulated tFCS signals for various illumination conditions and tracking localization errors. The reference-to-probe intramolecular dynamics was modeled as a mono-exponential relaxation (Ornstein-Uhlenbeck process) with a relaxation timescale of (**A**) 1 ms or (**B**) 10 ms, and a root mean squared distance (ref-to-probe RMSD) of 0, 17, 35 or 87 nm. $w = 310\,\mathrm{nm}$ is the diffraction limited probe beam waist at the focus. For all the simulation conditions, we simulated 10 molecules for 1 s each, with a probe dye fluorescence of 10^5 photons/s and a background noise of 10^4 photons/s. Plots from row 1, columns 1 and 4, and from row 4, column 4 in (A) are replotted from Fig. 2 for completeness, but show the signal of individual molecules rather that the mean (±95% CI) tFCS signal averaged across all the molecules.

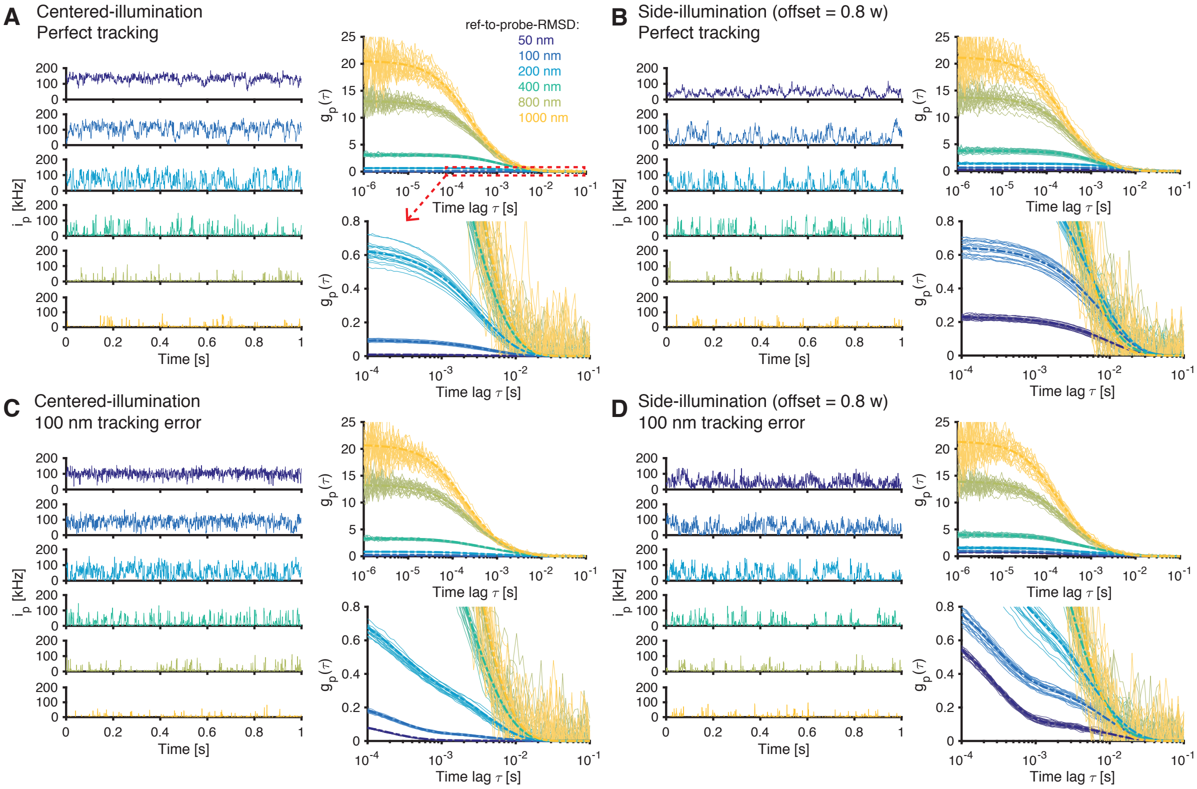

Figure S5. Intramolecular dynamics of large molecules - numerical simulations. Simulated tFCS data of molecules with a reference-to-probe dye root mean squared distance (ref-to-probe RMSD) of 50, 100, 200, 400, 800 and 1000 nm, showing that tFCS can resolve intramolecular dynamics at these length scales. The reference-to-probe dye dynamics was modeled as a mono-exponential relaxation (Ornstein-Uhlenbeck process) with a relaxation timescale of 10 ms. Simulations where done using the centered-illumination geometry (A and C) and side-illumination geometry (B and D, offset $1.0\,w$, where $w = 310$ nm), and with either perfect tracking (A and B), or 100 nm tracking localization error (C and D). For all four conditions, we simulated 10 molecules for 5 s each, with a probe dye fluorescence of 10^5 photons/s at the center of the probe beam, and a background noise of 2×10^4 photons/s (signal/noise = 5). In (A-D), the first 1 s of the probe intensity trace of a random molecule (left panel) and the fluorescence correlation signal of each individual molecule (top right panel, and zoom in on the shorter molecules at the bottom right) are shown. In all the simulations, the axial variation of the probe beam intensity was ignored to facilitate comparison between the simulated data and the theoretical predictions (dashed lines, Eq. 35). All the intensity traces and fluorescence correlation signals were background corrected (Eq. 17).

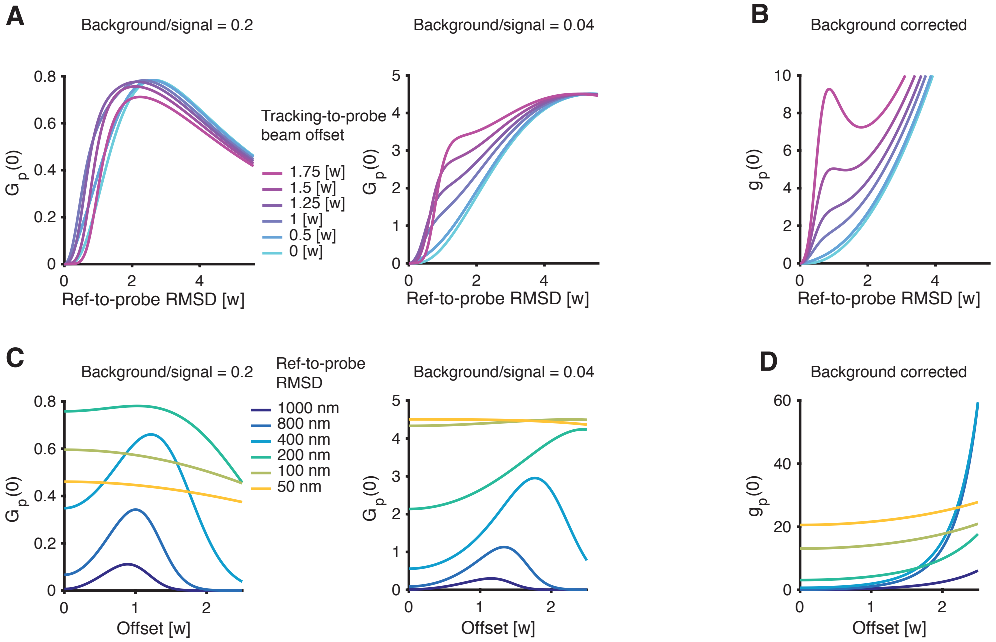

Figure S6. Amplitude of the tFCS signals as a function of the reference-to-probe fluctuation amplitude and the illumination offset. (A) Predicted amplitude of the raw fluorescence correlation signal $G_p(0)$ as a function the RMS amplitude of the reference-to-probe dye dynamics. Background/signal is defined as the ratio of the background intensity to the fluorescence intensity from the dye when it is located at the center of the probe laser. **(B)** Predicted amplitude of the fluorescence correlation signal $g_p(0)$ after background correction. These theoretical curves come from Eq. 35 and assume that the probe dye dynamics is isotropic with independent motions along the x, y, z axes. Blinking of the dye is ignored. **(C-D)** Predicted correlation amplitudes as in (A-B), but as a function of the tracking-to-probe beam offset. $[w]$ indicates that the length units are normalized with respect to the beam waist.

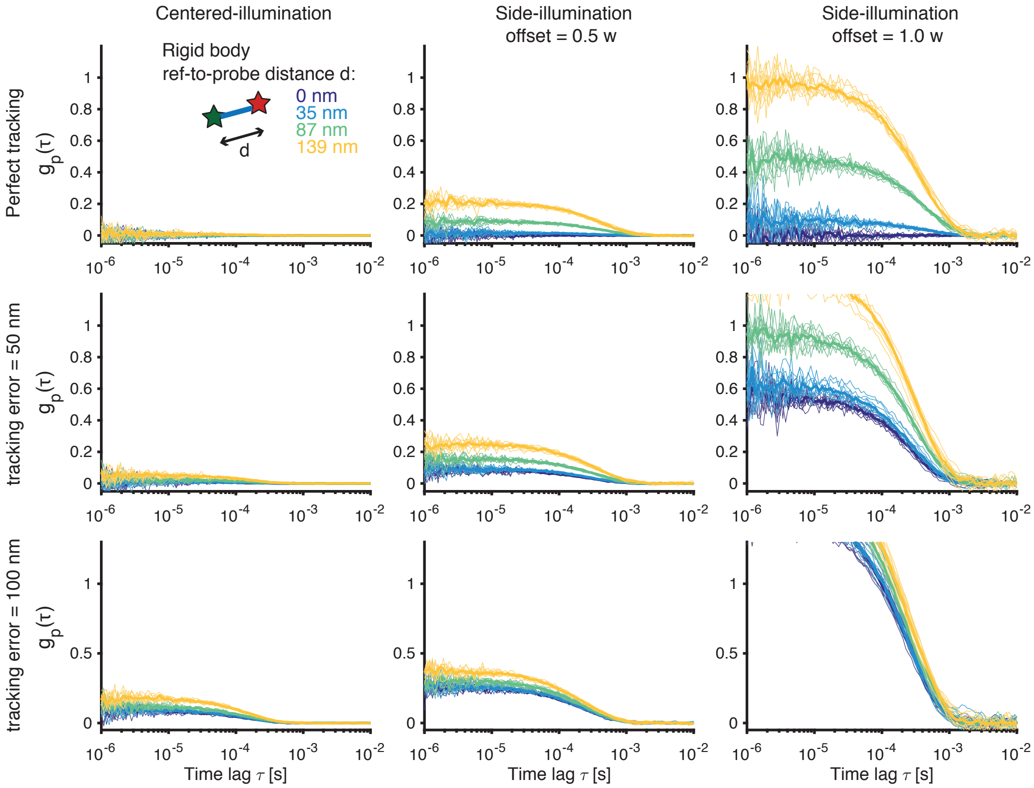

Figure S7. Spatial resolution of tFCS for measuring static distances – numerical simulation. Simulated tFCS signals of rigid molecules with a reference-to-probe dye distance of 0, 35, 87 or 139 nm, resulting from their rotational diffusion around the reference dye (the molecular tumbling is not constrained by the tracking feedback). We assumed a rotational diffusion timescale of 10 ms. For all of the simulation conditions, we simulated 10 molecules for 5 s each, with a probe dye fluorescence of 10^5 photons/s and a background noise of 10^4 photons/s. All of the intensity traces and fluorescence correlation signals were background corrected (Appendix, Eq. 17). Signals from individual molecules (thin lines) and population average (thick lines) are shown.

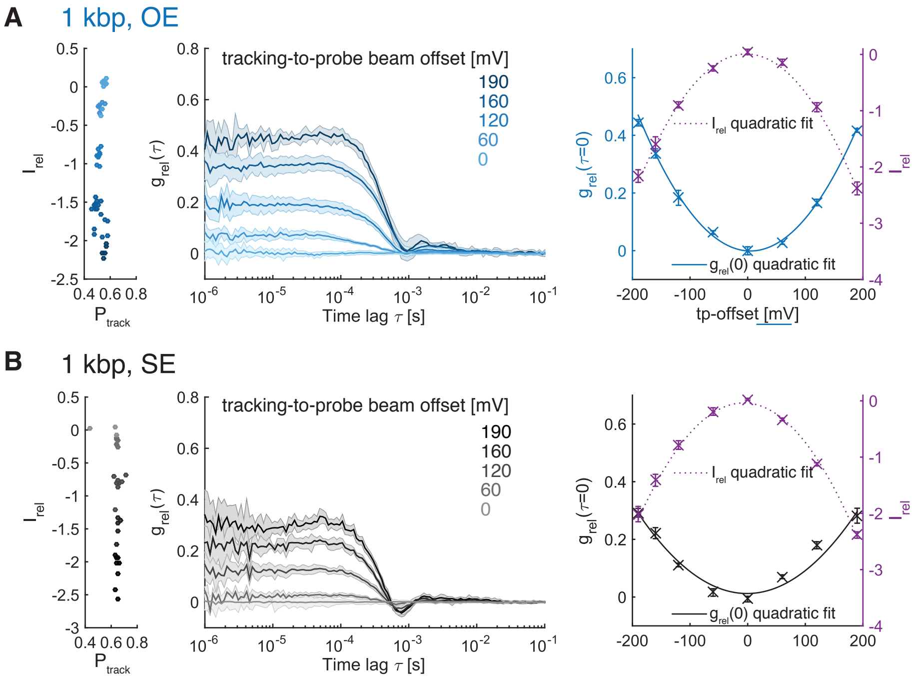

Figure S8. Effect of the tracking-to-probe beam offset on the relative fluorescence correlation functions. (**A**) Left: scatter plot of the relative intensity values I_{rel} as a function of the tracking laser power P_{track} for individual 1 kbp OE DNA molecules, measured using different tracking-to-probe beam offsets (increasing offsets in darker shades of blue). Middle: Relative correlation functions $g_{\mathrm{rel}}(\tau)$ for the same molecules (mean ± std), same color code as in left scatter plot. The relative correlation functions and intensities are computed by subtracting the side-illumination data of individual molecules from the average correlation function and intensities, respectively, across all molecules measured with the centered-illumination, using the expression of $g_{p,\mathrm{rel}}$ and I_{rel} (**SI Material and Methods** Eqs. 39 and 42). Right: Quadratic dependency of the relative correlation function amplitude and the relative intensity on the tracking-to-probe offset, shown as a quadratic fit of the data and as predicted by Eqs. 43 and 44). Crosses are sample median $\pm\,1.4826$ Median Absolute Deviation (MAD). (**B**) Same as in (A), but for 1 kbp SE DNA molecules.

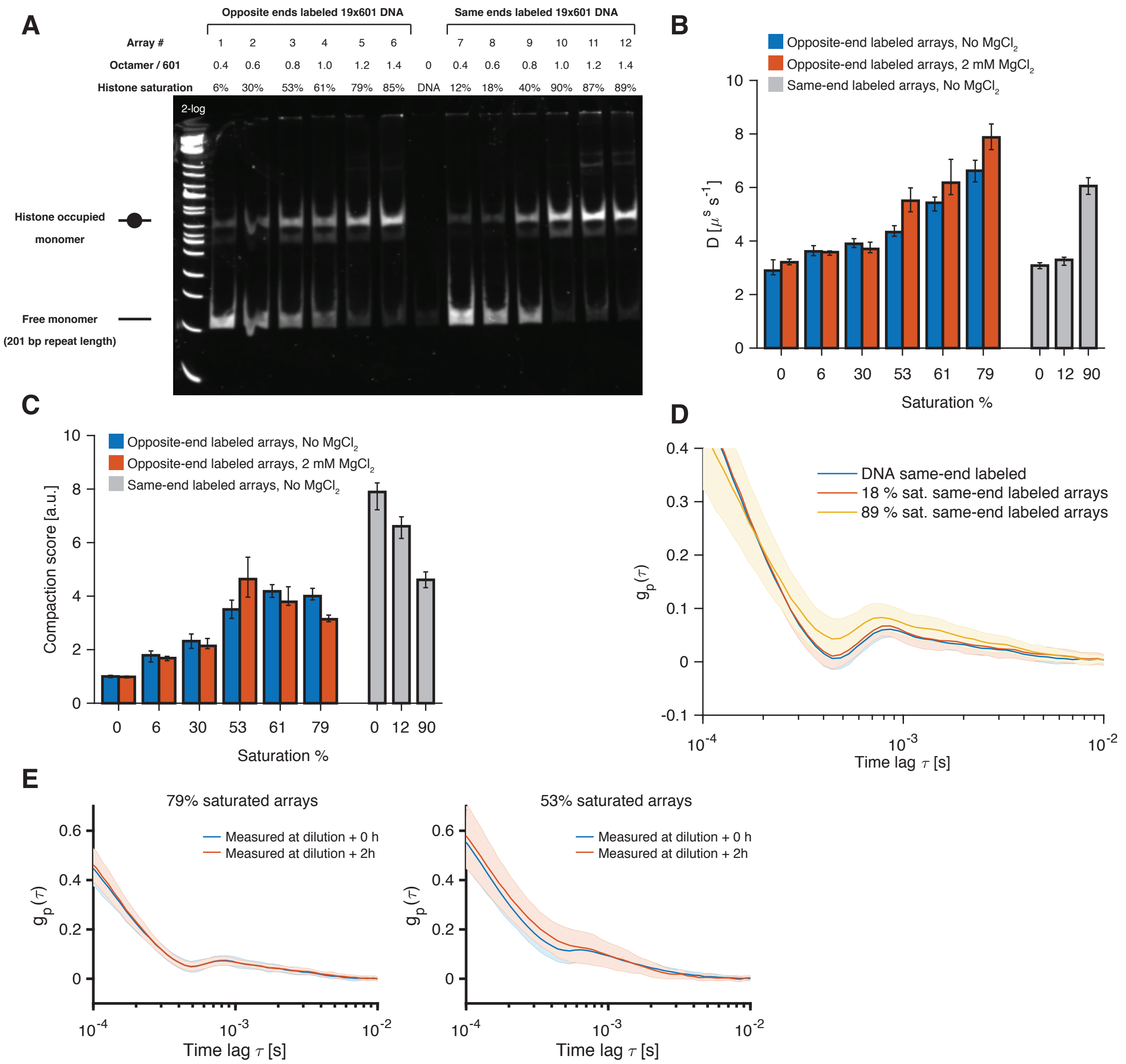

Figure S9. Characterization of nucleosome array saturation and stability, and of the tFCS noise floor for array compaction measurement. (A) Native-PAGE of nucleosome arrays after AvaI restriction digest. AvaI cuts in between each 201 bp long monomeric unit of the nucleosome positioning sequence (601 sequence). Not all arrays shown in this gel are measured by tFCS. **(B-C)** Median (±95% bootstrap confidence intervals) diffusivity (B) and compaction score (C) of DNA and nucleosome arrays. From left to right: bare DNA labeled with the reference and probe dyes on opposite ends, arrays #1-5 (labeled on opposite ends) before (blue) and after (red) addition of 2 mM magnesium, bare DNA labeled with the reference and probe dyes on the same ends, and arrays #7 and #10. Data for bare DNA and arrays are reproduced from **Fig. 4**. **(D)** tFCS signals of control DNA and arrays labeled on the same ends. The increase in tFCS amplitude and corresponding decrease in compaction score for the 79% saturated array is due to an increase in tracking error as a result of faster diffusion. **(E)** Stability of nucleosome arrays during single molecule tracking. tFCS signals (population media ± std.) of 79% and 53% saturated arrays recorded immediately after dilution to the tFCS concentration (1 pM in labeled arrays), or 2 h after dilution.

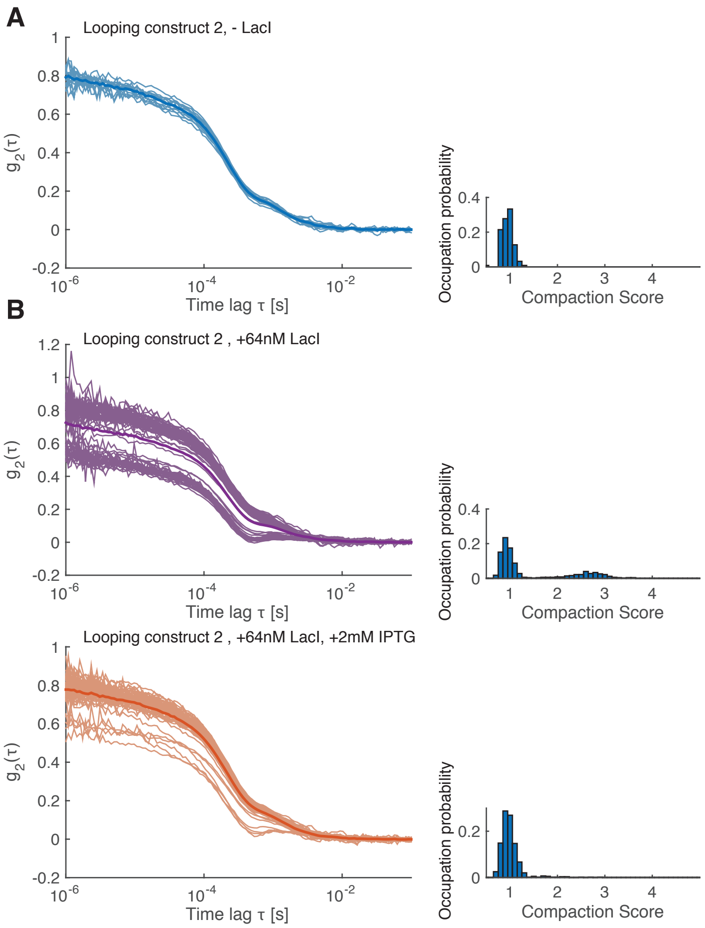

Figure S10. IPTG prevents the formation of LacI-induced DNA loops. (**A**) tFCS signals of individual DNA molecules from the looping construct 2 (**Table S1**) in absence of LacI (left) or after 5 minutes incubation with 64 nM LacI (middle), followed by addition of 2 mM IPTG (right). (**B**) Distribution of the compaction score for the three conditions in (A).

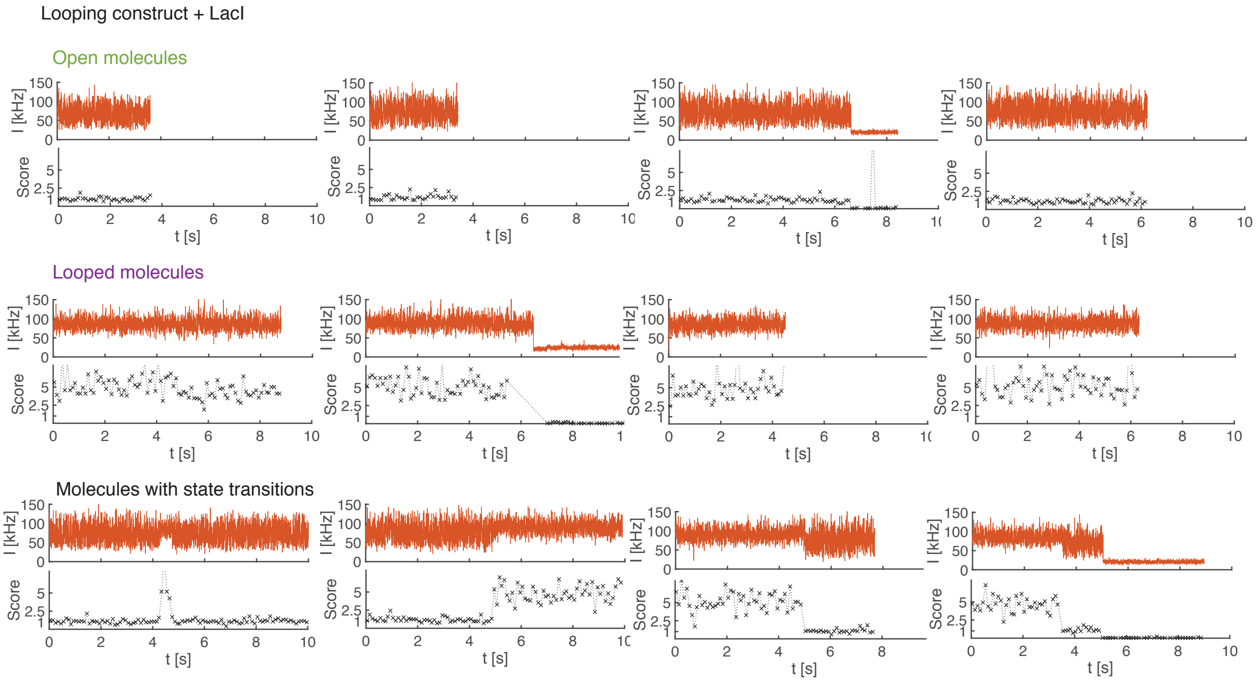

Figure S11. Examples of molecules in the looped and open conformations, and examples of transitions between the two states. Recordings of individual molecules from the looping constructs. For each molecule, the fluorescence intensity from the probe dye is shown binned at 3 ms (top plot), and the trajectory of the compaction score is shown binned at 100 ms (bottom plot).

Oligos	**Sequence**	**Source**
#118	**CTAG**AATTGT GAGCGGATAA CAATTACACC ACCATACCGT GTCTCG	IDT
#120	**AATT**AAaTGT GAGCGagTAA CAAccGTCAA GCACTGGAAC GTCGAG	IDT
#132	/5Phos/ AATTGTTATC CGCTCACAAT T	IDT
#133	/5Phos/ ggTTGTTAct CGCTCACAtT T	IDT
#140	AATTACACCA CCATACCGTG TCTCGAAaTG TGAGCGagTA ACAAccGTCA AGCACTGGAA CGTCGAG	IDT
#141	/5Phos/ GGCTGTACGT GTGGAATCAG AAGTGGCCGC GCGGCGGCAG TGCAGGCT	IDT
	CTAGAGCCTG CACTGCCGCC GCGCGGCCAC TTTTGAGTCC ACACTTACAA CCACACCACC	
#142	ATACCGTGTC TCG	IDT
Primers	**Sequence**	**Source**
#P1	/5Biosg/ CTCGACGTTC **/iUniAmM/** CAGTGCTTGAC	IDT
#P2	CGAGACACGG **/iUniAmM /** TATGGTGGTGT	IDT
#P3	/5Biosg/ CTCGACGTTC **/iCy3b/** CAGTGCTTGAC	Labeled #P1, gel purified
#P4	CGAGACACGG **/iATTO647N /** TATGGTGGTGT	Labeled #P2, gel purified
#P5	CGAGACACGG **/iAlexa647 /** TATGGTGGTGT	Labeled #P2, gel purified
Geneblocks	**Sequence**	**Source**
Geneblock	1 CCATTCTGCC TGGGGACGTC GGAGCGATAT C**CGAGACACG GTATGGTGGT GT**GCTAGCTC 61 TCATCTCACG CAGTCCGC**AA TTGTGAGCGG ATAACAATT**G ATTGTGCGAG ACAATGCTAC 121 CTGCAGGGGC CTAGGCGGGC GAGGCTGCTC CCACCAGCAG GGGGCGCTTT GACTCGCATG 181 CCCTTACCGG TCGGAACTCG A**GAATTC**GGC GCGCCGACAG ATCTCTGGAG AATCCCGGTG 241 CCGAGGCCGC TCAATTGGTC GTAGCAAGCT CTAGCACCGC TTAAACGCAC GTACGCGCTG 301 TCCCCCGCGT TTTAACCGCC AAGGGGATTA CTCCCTAGTC TCCAGGCACG TGTCAGATAT 361 ATACATCCTG TCCTCGAGC**T CTAGA**CGCTC AGCCTCACTA CTCATACTAG TAGTCACCAC 421 TGCCGCCTCT CGGCCATTTC CGTCTCCACA GCCACAACCA AGCTTTCGGT TGAACTCTAT 481 CACGCCCATG G**AAATGTGAG CGAGTAACAA CC**GGATCCCT GGTCTTCGAA GTTAGCACAC 541 GCGT**GTCAAG CACTGGAACG TCGAG**GATAT CCCCTATAGT GAGTCGTATT ACGTAG	IDT
Capping fragments	**Sequence**	**Source**
Cap1	Anneal : #118 + #132 + #P4	Annealed
Cap2	Anneal : #120 + #130 + #P3	Annealed
Cap3	Anneal : #140 + #133 + #P3 + #P4	Annealed
Cap4	Anneal : #141 + #142	Annealed
Cap5	Anneal : #118 + #132 + #P5	Annealed
Sequence aliases	**Sequence**	
R0	1 CGAGACACGG /iATTO647N / TATGGTGGTG T	
R5	1 CTCGACGTTC /iCy3b/ CAGTGCTTGA C	
LacO1	1 AATTGTGAGC GGATAACAAT T	
LacO2	1 AAATGTGAGC GAGTAACAAC C	
LacOsym	1 AATTGTTATC CGCTCACAAT T	
DNA constructs	**Sequence**	**Source**
0.5 kb SE	Cap 3 + (391 bp from random plasmid digestion with XbaI EcoRI) + Cap 4	Ligation + gel purification
1.0 kb SE	Cap 3 + (898 bp from random plasmid digestion with XbaI EcoRI) + Cap 4	Ligation + gel purification
3.9 kb SE	Cap 3 + (3792 bp from random plasmid digestion with XbaI EcoRI) + Cap 4	Ligation + gel purification
0.5 kb OE	Cap 1 + (391 bp from random plasmid digestion with XbaI EcoRI) + Cap 2	Ligation + gel purification
1.0 kb OE	Cap 1 + (898 bp from random plasmid digestion with XbaI EcoRI) + Cap 2	Ligation + gel purification
3.9 kb OE	Cap 1 + (3792 bp from random plasmid digestion with XbaI EcoRI) + Cap 2	Ligation + gel purification
6.1 kb OE	Cap 1 + (5992 bp from random plasmid digestion with XbaI EcoRI) + Cap 2	Ligation + gel purification
LacO looping	R0 - (20 random bp) - LacO1 - (~2600 random bp) - LacOsym - (random 32 bp) - R5'	PCR R0 and R5' primers
LacO lasso	R0 - (20 random bp) - LacO1 - (~1300 random bp) - LacO1 - (~random 1300 bp) - R5'	PCR R0 and R5' primers
LacO 3 sites	R0 - (20 random bp) - LacO1 - (~1300 random bp) - LacO1 - (~random 1300 bp) - LacOsym - (random 32 bp) -	PCR R0 and R5' primers
LacO looping 2	R0 - (20 random bp) - LacO1 - (2608 random bp) - LacO2 - (random 32 bp) - R5'	PCR R0 and R5' primers
19x601 kb for	Cap 5 + (19x601 array with XbaI EcoRI overhangs) + Cap 2	Ligation + gel

Prime (') indicates reverse complement

Table S1. DNA constructs and oligonucleotides used in this study.

Experiment #1	**DNA end-to-end dynamics**						
Illumination conditions	Centered-illumination, Side-Illumination						
Detector config.	P/P						
Dyes	Cy3b, Atto647 N						
Sample	**# mol. group 2**	**# included**	**median(T) [s]**	**std(T) [s]**	**max(T) [s]**	**median(Nphotons)**	**std(Nphotons)**
487 OE, centered illum.	17	15	3.5	2.0	13.1	459759.0	206.3
994 OE, centered illum.	8	8	3.4	1.0	9.0	438878.0	180.8
3888 OE, centered illum.	5	3	4.0	3.1	6.1	387648.0	293.7
487 SE, centered illum.	27	27	2.8	1.5	13.2	347900.0	174.7
994 SE, centered illum.	3	3	2.5	1.3	3.4	365077.0	199.3
3888 SE, centered illum.	10	8	4.1	3.5	13.2	633710.0	554.5
487 OE, centered illum.	17	15	2.8	1.1	9.9	159709.0	60.2
994 OE, side illum.	18	15	4.1	2.6	8.3	239249.0	143.3
3888 OE, side illum.	9	8	8.8	6.5	14.2	504698.0	385.9
487 SE, side illum.	25	19	3.7	3.1	10.2	206416.0	176.8
994 SE, side illum.	6	5	2.2	1.5	8.7	148137.0	113.7
3888 SE, side illum.	13	11	4.8	5.0	10.4	353416.0	373.4
Experiment #2	**Nucleosome arrays**						
Illumination conditions	Side-Illumination						
Detector config.	R/P						
Dyes	Cy3b, Alexa647						
Sample	**# mol. group 2**	**# included**	**median(T) [s]**	**std(T) [s]**	**max(T) [s]**	**median(Nphotons)**	**std(Nphotons)**
19x601 DNA	34	32	1.98	1.11	6.20	78998.0	45742.00
19x601 DNA +2mM Mg	55	47.00	3.08	1.76	9.69	138900.0	86216
Arrays 6% saturation	82	68.00	2.02	1.41	9.65	86103.0	56038
Arrays 6% saturation +2mM Mg	120	100.00	2.75	1.69	12.52	126140.0	75604
Arrays 30% saturation	81	70.00	1.56	0.73	4.01	57540.0	28062
Arrays 30% saturation +2mM Mg	71	56.00	2.53	1.71	20.52	122190.0	94445
Arrays 53% saturation	98	83.00	1.78	1.21	8.85	85243.0	59737
Arrays 53% saturation +2mM Mg	15	11.00	3.10	2.24	5.83	115250.0	104480
Arrays 61% saturation	62	51.00	1.51	1.03	6.38	62519.0	41064
Arrays 61% saturation +2mM Mg	26	20.00	2.44	1.74	6.86	129170.0	95436
Arrays 79% saturation	53	44.00	2.30	1.68	7.38	87780.0	71750
Arrays 79% saturation +2mM Mg	64	52.00	2.83	2.46	10.21	141130.0	129190
19x601 DNA same-end labeling	85	68.00	2.19	1.17	11.15	92625.0	62383
Arrays same-end 18% saturation	94	86.00	1.71	0.81	8.41	67040.0	30977
Arrays same-end 90% saturation	91	76.00	1.59	0.84	7.67	76134.0	40472
Experiment #3	**LacI induced looping**						
Illumination conditions	Side-Illumination						
Detector config.	R/P						
Dyes	Cy3b, Atto647 N						
Sample	**# mol. group 2**	**# included**	**median(T) [s]**	**std(T) [s]**	**max(T) [s]**	**median(Nphotons)**	**std(Nphotons)**
2.5 kb SE	31	29	2.8	1.4	9.9	212208.0	116222.0
LacO Looping -LacI	8	7	4.1	1.8	9.2	216523.0	90544.7
LacO Looping +LacI	61	61	3.5	2.6	15.3	193024.1	170208.5
LacO Lasso +LacI	64	64	3.1	2.3	16.5	171235.0	123537.9
LacO 3 sites +LacI	32	32	2.6	1.8	9.8	164863.3	129426.1
LacO Looping 2 - LacI	14	14	2.8	1.1	14.2	206329.4	101200.1
LacO Looping 2 +LacI	65	65	3.2	2.2	13.3	225997.9	150074.2
LacO Looping 2 +LacI +IPTG	59	59	4.1	2.9	24.4	306211.2	248106.0

Table S2. Experimental conditions and tracking statistics.